Weathering Products of a Dismantled Variscan Basement. Minero-Chemical Proxies to Insight on Cretaceous Palaeogeography and Late Neogene Palaeoclimate of Sardinia (Italy)

Paola Mameli[1]*, Giovanni Mongelli[2], Rosa Sinisi[2] and Giacomo Oggiano[1]

[1] Department of Chemistry and Pharmacy, University of Sassari, Sassari, Italy, [2] Department of Sciences, University of Basilicata, Potenza, Italy

This study compares, for the first time, the mineralogy and geochemistry of two residual-clay deposits in NW Sardinia (Nurra district) that formed at different times in tropical and sub-tropical climates. Both deposits represent palaeosols with deep-weathered residual profiles and overlie Mesozoic carbonate rocks that were deposited on the south European palaeomargin. The older alterite is Cenomanian–Turonian in age and grades upward into a horizon of karstic bauxite, whereas the younger unit occurs within alluvial deposits of Late Neogene age. The Cretaceous palaeosol represents the precursor of the overlying bauxite and formed from unknown sedimentary parent rocks. In contrast, the Messinian weathering products formed by alluvium that was sourced from the Variscan metamorphic basement. Chemical Index of Alteration values, REE fractionation index values, and the results of R-mode factorial analysis suggest a common initial weathering path and a common precursor for the deposits. However, the latter stages of weathering of the Cretaceous palaeosols resulted in lateritic alteration and bauxite production, whereas weathering of the Late Neogene palaeosols produced 2:1 clay minerals under less extreme conditions. Comparison of these residual products constrains the parental material and weathering trends and allows insight into the relationship between palaeoclimate and regional/local palaeogeography of southern Europe during Upper Cretaceous and during Messinian.

Keywords: clays, chemical index of alteration, variscan basement, Cretaceous, Messinian

INTRODUCTION

Breakdown of rock at the Earth's surface produces a thin porous covering that represents a section of the recently defined "Critical Zone" (National Research Council, 2001; Brantley et al., 2006), and according to Eggleton (2001), referred to as "regolith." Typical regolith displays considerable vertical (distinguishable layers of weathered rocks) and lateral (variations in landscape and associated soils) heterogeneity (Taylor and Eggleton, 2001; Anderson et al., 2007). The rate and intensity of chemical weathering are controlled by various factors (Singer, 1984; Garzanti and Resentini, 2016), including vegetation, drainage of the parent rock, and climate.

Weathering products such as clays are an important component of clastic sediments (e.g., siltstone, shale, and greywacke) and can record the environmental conditions of the source area (Zabel et al., 2001; Sinisi et al., 2014).

Clay mineral assemblages in residual and transported sediments are controlled primarily by climatic conditions. Soils and sediments at high latitudes and in cold climates generally experience a low rate of chemical weathering that results in the production of illite and chlorite association (Robert and Maillot, 1990; Ehrmann and Mackensen, 1992; Ehrmann et al., 2005). Conversely, soils and terrigenous sediments in tropical wet regions undergo heavy leaching that produces kaolinite and gibbsite assemblages (Macias Vazquez, 1981; Deepthy and Balakrishnan, 2005; Bauluz et al., 2014). Furthermore, the degree of weathering controls the accumulation/leaching of elements from the precursor rocks to the residual material (Net et al., 2002). Different elements show varying behavior during chemical weathering. The low field strength elements (LFSE; e.g., Na, Ca, and Sr) have a high affinity for aqueous phases and are therefore easily removed from exposed rocks in wet regions (Nesbitt et al., 1980; Nesbitt and Markovics, 1997). Other elements, such as K, Rb, Mg, and Ba, are easily removed from primary minerals but are often rapidly incorporated into secondary clay minerals and insoluble hydroxides within weathering profiles and residual deposits. Chemical weathering therefore redistributes major and trace elements in rocks, particularly in sedimentary deposits. During weathering, some elements are depleted in the parent rock and residual products, whereas others are conservative and are retained in moderately weathered rocks or concentrated in residual deposits (Nesbitt et al., 1980; Peuraniemi and Pulkkinen, 1993; Condie et al., 1995; Nesbitt and Markovics, 1997). Hence, mineralogical and geochemical investigations of alterites (including palaeosols) can constrain both the palaeoclimate and the nature of the parent rocks.

The present study compares the mineralogical and geochemical features of two weathering products that were generated at different times on the south European crust (Sardinia-Corsica microplate).

In NW Sardinia (Nurra district), alterites overlie Mesozoic carbonates and occur in two distinct stratigraphic contexts. The older alterite deposit is overlain by Upper Cretaceous karstic bauxites and rests above Upper Jurassic/Lower Cretaceous carbonates. In contrast, the younger alterites occur as palaeosols within a continental sequence of alluvial fan and braided river deposits, late Miocene in age, which also overlie the same Mesozoic carbonate sediments.

Between Lower and Upper Cretaceous, clayey alterites and associated bauxite formed in a monsoonal climate on the south European palaeomargin at 30°N palaeolatitude (Dercourt et al., 1985; Mameli et al., 2007). The major questions on this clayey material associated to bauxite are concerned with its precursor. Indeed, the dissolution of high-grade carbonates is unlikely to have generated the observed thick continuous layer of karstic bauxite. Accordingly, it has been proposed that the bauxite was derived from allochthonous debris, deposited on Mesozoic limestone (MacLean et al., 1997), which in turn may have been sourced from Variscan basement (Mameli et al., 2007). This hypothesis, if confirmed, is consistent with an Upper Cretaceous palaeogeographic setting in which portions of the carbonate shelf were uplifted and eroded causing the basement to be exposed. In contrast, the precursor of the Messinian alterites is known to be debris derived from the Variscan metamorphic basement of NW Sardinia (Mongelli et al., 2012), but what is still uncertain is the palaeoclimate during the age of their formation.

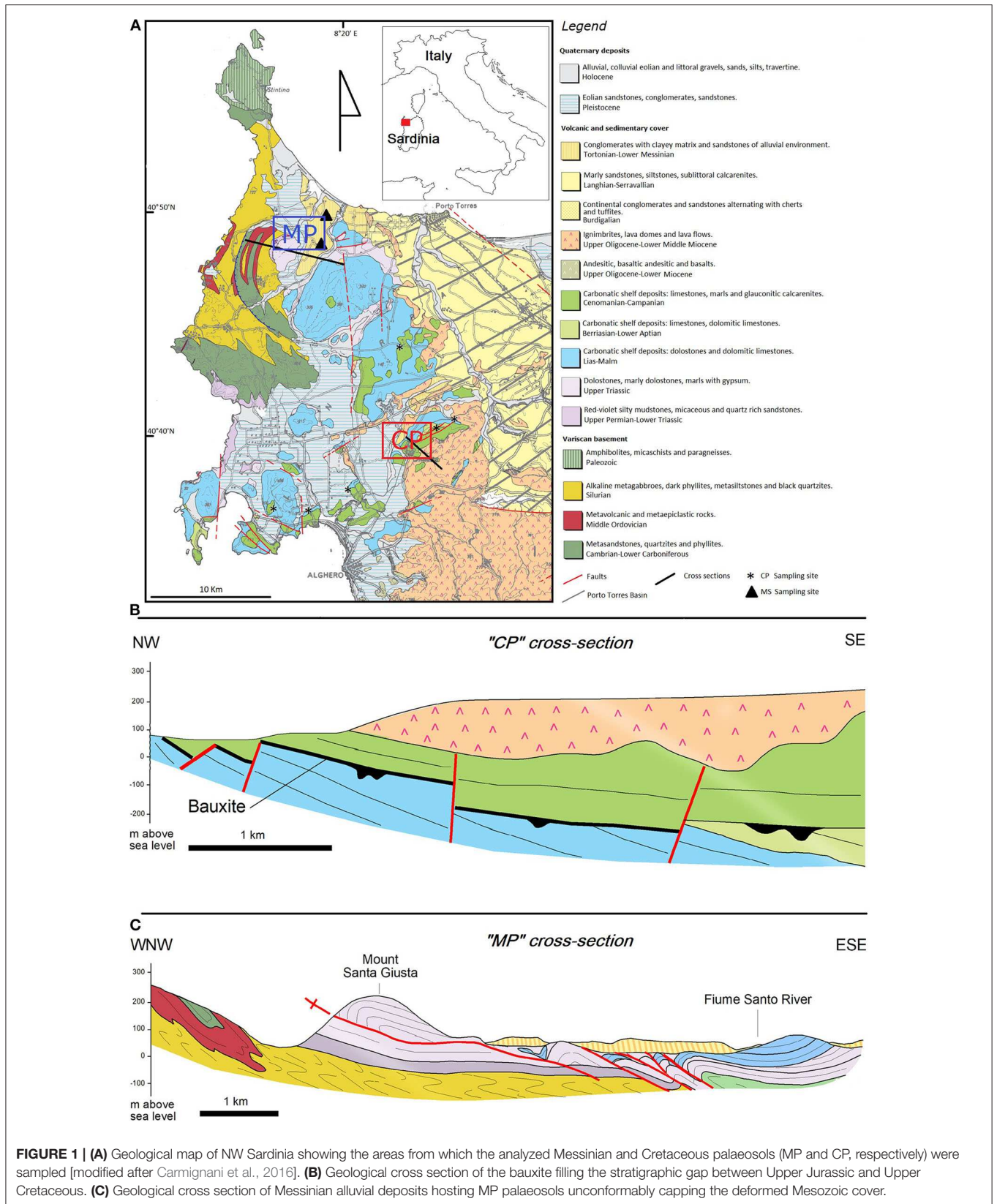Messinian is an age known for the so called Mediterranean salinity crisis (MSC—i.e., its partial desiccation), one of the most appealing and debated palaeoclimatic and palaeogeographic events in the geological history of this sea. It is still controversial whether the desiccation is controlled by climatic or tectonic factors (Fauquette et al., 2006; Achalhi et al., 2016). Most of palaeoclimatic and palaeogeographic reconstructions are based on palynological and isotopic data on continental and marine sediments, respectively (Fauquette et al., 2006; Jiménez-Moreno et al., 2013; Bertini and Menichetti, 2015). The attempts to test the geochemical and mineralogical proxies on weathering product are scanty (Mongelli et al., 2012) and are worthy of further investigations able to give hints of palaeoclimatic relevance.

By comparison between the mineralogy and geochemistry of the two alterites, we are expected to disclose new aspects in Cretaceous palaeogeography and contribute in the assessment of Messinian palaeoclimate.

In detail we aim to provide further insights into: (1) the provenance of the Cretaceous alterite, which is the parental material of bauxite; (2) the palaeogeography of the south European margin during the Late Cretaceous; (3) the palaeoclimatic conditions in the western Mediterranean during the Messinian. Overall we also aim to contribute to our understanding of the interplay among palaeoclimate and precursor material during the weathering of Al-rich rocks to clay.

GEOLOGICAL SETTING

The Sardinian microplate was part of the South Europe margin until the Aquitanian (Carmignani et al., 2004), before its counter-clockwise drift and the opening of the Ligurian-Provencal Basin in Burdigalian time (Thomas and Gennesseaux, 1986; Gattacceca et al., 2007; Oudet et al., 2010). NW Sardinia (**Figure 1A**) is characterized by a structural high caused by the tilting of the Ligure-Provencal rift shoulder, during early Miocene. In present coordinates the tilting results toward the east; progressively older formations are therefore exposed toward the west. The oldest rocks crop out near the coast and comprise mainly phyllite with intercalated metarhyolite and metabasite of the Variscan basement, which northward, due to the prograde metamorphism, pass into gneiss, amphibolite, and anatectic granite (Oggiano and Mameli, 2006; Cuccuru et al., 2018). Late Permian and Mesozoic cover units are exposed along a hilly/flat area to the east of the basement. Farther east, the Mesozoic cover is overlain by Tertiary (Aquitanian–Langhian) volcano-sedimentary successions of the Porto Torres Basin (Funedda et al., 2000). The Mesozoic marine succession is almost continuous from the Triassic (Ladinian) to the uppermost Cretaceous (Campanian) and comprises evaporite,

FIGURE 1 | (A) Geological map of NW Sardinia showing the areas from which the analyzed Messinian and Cretaceous palaeosols (MP and CP, respectively) were sampled [modified after Carmignani et al., 2016]. **(B)** Geological cross section of the bauxite filling the stratigraphic gap between Upper Jurassic and Upper Cretaceous. **(C)** Geological cross section of Messinian alluvial deposits hosting MP palaeosols unconformably capping the deformed Mesozoic cover.

dolostone, and limestone, with few intercalations of marlstone. There exists a stratigraphic gap embracing the Albian–Turonian interval, related to a period of emergence (Mameli et al., 2007). This gap is represented by an almost continuous horizon of karstic bauxite, and. it is constrained, on paleontological and micropaleontological bases (Philip et al., 1978; Philip,
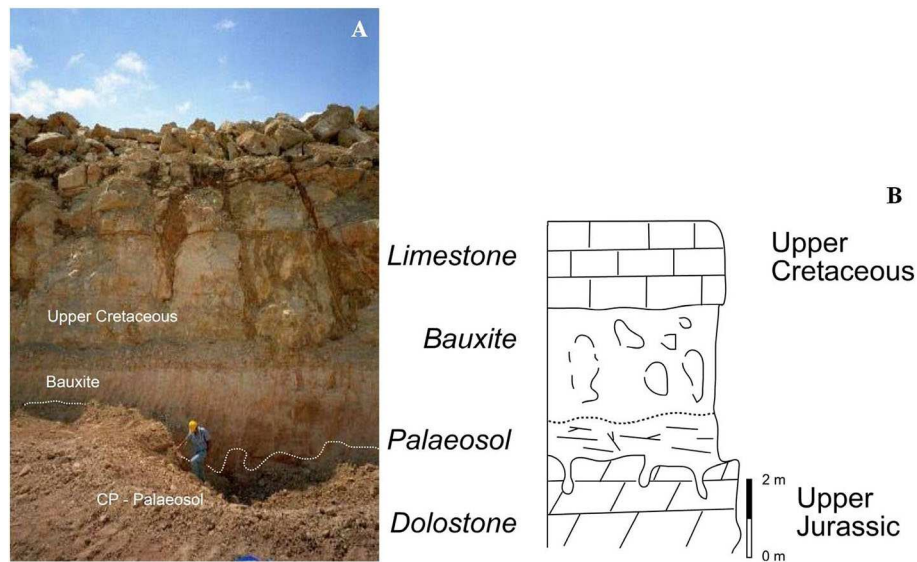
FIGURE 2 | (A) Clay-bearing CP palaeosol below bauxite at Olmedo mine. **(B)** Schematic stratigraphy of the Cretaceous deposits.
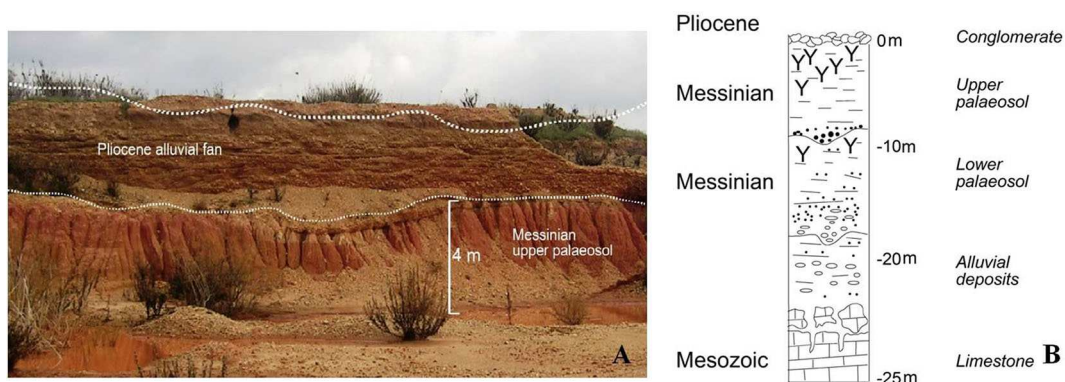

FIGURE 3 | (A) Continental deposit comprising channelized gravel and clay-rich horizons displaying evidence of pedogenesis (modified after Mongelli et al., 2015). **(B)** Sketch of the stratigraphy of the MP deposit.

1983) between the Aptian and the Coniacian. The bauxite unconformably overlies different rocks of different ages of the Mesozoic carbonate shelf that include pure limestone, dolostone, and minor marlstone (**Figures 1B**, **2A,B**). Below the bauxite, green-gray and purple clay horizons locally occur, which display a mottled appearance and contain carbonaceous remnants of fossil plants. These clays are interpreted as palaeosols, where the green-gray portions with scattered carbonized vegetal remnants could represent reworked humic horizons. The passage into the overlying bauxite is gradational, marked by lowering in kaolinite, increasing Al_2O_3 and appearance of pisolites (Mameli et al., 2007).

The Messinian palaeosols are embedded within a wide alluvial system that linked up with upstream basement areas. The alluvial deposits unconformably overlie Mesozoic carbonate rocks that are underlain by Permian clastic sediments, which are the oldest, deposited on the Variscan basement (**Figure 1C**). Interbedded channelized debris contains pebbles of metamorphic quartz, schist, and quartzite, consistent with being sourced from the adjacent basement. The alluvial deposit is locally several tens of meters thick (**Figure 3A**) and, together transported clay, hosts at least two horizons of residual clays, which feature as palaeosols. The primary palaeosol is well exposed along road cuts and quarries, and has a maximum thickness of 10 m. Another palaeosol horizon, which was intersected during coring and in one excavation, is generally separated from the former by a discontinuous gravelly/sandy deposit (**Figure 3B**). In the excavation the transition between the two palaeosols is a horizon of fine sands that yielded a tusco-sardinian land mammal palaeofauna of Turolian age, leading to consider as Messinian the upper palaeosol (Abbazzi et al., 2008).

The upper palaeosol consists of reddish clay (5/8–2Y; mottled with gray in reduced areas) to ochre (8/8–7.5Y) with rare rhizoliths (**Figure 4**), and locally is cut by overlying, channelized
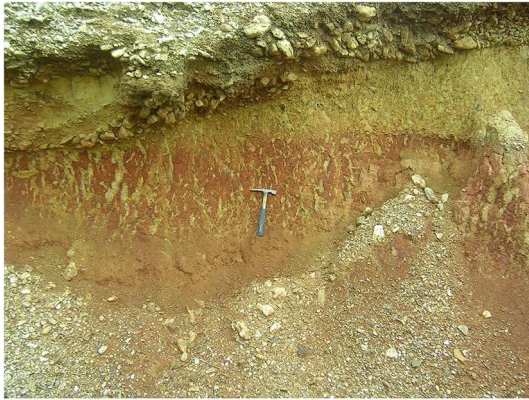
FIGURE 4 | Rhizoliths within pedogenized clay (Mongelli et al., 2015).

quartz-bearing gravel deposit. This deposit consists of mild sorted, quartz-dominated gravel, clast supported, with no matrix or with fine sandy matrix. The gravel clasts are sub-rounded to sub-angular. The particle size ranges from 1.2 cm pebbles to 10–15 cm, cobbles in places cemented by manganese oxyhydroxides. This poorly graded, relatively disorganized sediment can be referred to streamflows-dominated alluvial fan, possibly of Pliocene age.

MATERIALS AND METHODS

We performed mineralogical and geochemical analyses on 34 representative samples: 12 from the Cretaceous palaeosols (CP) and 22 from the Messinian palaeosols (MP). CP samples were collected in two vertical profiles (3 per each profile from bottom up to the boundary with bauxite) in a mined open pit, other 6 come from individual surficial outcrops scattered over a wide area, in order to get samples representative of different Mesozoic bedrocks. The upper Messinian palaeosol was sampled in two quarry cuts (samples MP1–MP12) at different levels, the lower (MP 13–MP 22) in two cores drilled during brick clay prospecting.

Whole-rock samples were dried and reduced to fine powder in a planetary mill (Retsch) equipped with two agate jars and agate milling balls. Mineralogical analysis was performed on randomly oriented whole-rock powders using a Siemens D5000 powder X-ray diffractometer (Cu-Kα radiation, 40 kV, and 30 mA) at 2θ angles of 6–70° and a step size of 0.02°. Mineral phases were identified from powder XRD patterns using the ICDD PDF-2 database and the Bruker DIFFRACplus EVA 14.2 software package.

Major, trace, and rare earth element concentrations were measured by inductively coupled plasma–optical emission spectrometry (ICP-OES) and inductively coupled plasma–mass spectrometry (ICP–MS) at Activation Laboratories, Ancaster, Canada. The powder samples were dissolved by fusion with lithium metaborate/tetraborate and the resulting molten bead was rapidly digested in a weak nitric acid solution or a multiacid one (for Cu, Zn, and Ni determination), as expected from 4Litho and 4B1 packages. GXR-1, NIST 694, DNC-1, GXR-4, SDC-1, GXR-6, LKSD-3, TDB-1, NOD-P-1, W-2a, DTS-2b, SY-4, CTA-AC-1, BIR-1a, NCS DC86312, ZW-C, NCS DC70009 (GBW07241), OREAS 100a (Fusion), OREAS 101a (Fusion), OREAS 134a (Fusion), and JR-1 were the standards used. Analytical uncertainties were <5%, except for elements occurring at concentrations of ≤10 ppm, which yield uncertainties of 5–10%. Loss on ignition (LOI) was estimated using gravimetric analysis following combustion at 950°C.

The texture, mineralogy, and microchemistry of polished sections of representative samples were analyzed using an ESEM Zeiss LaB6 scanning electron microscope equipped with an energydispersion spectrometer (EDS).

The samples were then labeled according to their provenance.

The degree of weathering of the palaeosols was estimated through calculation of the chemical index of alteration (CIA = $Al_2O_3/(Al_2O_3 + CaO^* + Na_2O + K_2O) \times 100$; where elements are in molecular proportions and CaO* represents CaO hosted in silicate minerals only; Nesbitt and Young, 1982). CIA values were not calculated for samples with CaO concentrations higher than that of Post Archaean Australian Shales (PAAS) (1.3 wt.%; Taylor and McLennan, 1985).

Inter-elemental relationships were determined using element variation diagrams and R-mode factor analysis, performed with XLStat software package. In detail we used varimax rotation and subsequent R-mode factor analysis using principal components in the two sets of palaeosol samples. A standardized correlation matrix with equal weighting for all variables was used, enabling conversion of the principal component vectors into factors. Factor weightings were determined separately for the Cretaceous and Messinian samples. For both datasets, we only discuss those variables with absolute weightings of >0.65.

RESULTS

Mineralogy

XRD patterns from whole-rock disoriented powders indicate that all samples are composed of dominantly clay minerals and quartz, with minor Al and/or Fe-oxyhydroxides and Ti-oxides.

The main mineral assemblage in the CP samples comprises clay minerals (kaolinite + illite ± montmorillonite) + quartz + Al/Fe-oxyhydroxides (boehmite/gibbsite + goethite + minor hematite) + Ti-oxides (anatase and/or rutile) (**Figure 5**).

The main mineral assemblage in the MP samples comprises clay minerals (illite + kaolinite) + quartz + Al/Fe-oxyhydroxides (gibbsite + goethite) + Ti-oxides (rutile + minor anatase) ± feldspar. Palygorskite occurs in three core samples from the lower palaeosol and halite was detected in four samples (**Figure 6**).

The minerals phases are generally well- resolved except for some Cretaceous samples from Olmedo mine and some core samples from the Messinian deposit.

In addition to XRD, SEM EDS observation evidenced: (i) the occurrence of tiny bipyramidal magnetite crystals in the Al rich MP1 and MP2 samples; (ii) the coexistence of detrital, irregularly edged, kaolinite plates with tiny, exagonal, growing crystal stacks; (iii) the survival of detrital muscovite laminae in some quartz rich millimetric layers within the upper Messinian palaeosol; (iv) the occurrence of detrital kaolinite also in the Cretaceous clays.

Chemistry

The major and trace element concentrations of the analyzed sets of samples are listed in **Table 1**. Major elements and their variability are summarized below.

CP samples yield SiO$_2$ concentrations of 32.09–43.94 wt.% (mean = 39.10 wt.%; n = 12), indicating depletion relative to the Upper Continental Crust (UCC) [66.62 wt.%; (Rudnick and Gao, 2014) and references therein] and post-Archaean Australian shale (PAAS) (62.80 wt.%; Taylor and McLennan, 1985). The samples contain 23.44–31.64 wt.% Al$_2$O$_3$ (mean = 26.98 wt.%), more than the UCC (15.40 wt.%) and PAAS (18.90 wt.%). They contain 7.90–17.24 wt.% Fe$_2$O$_3$ (mean = 12.77 wt.%), 0.25–4.28
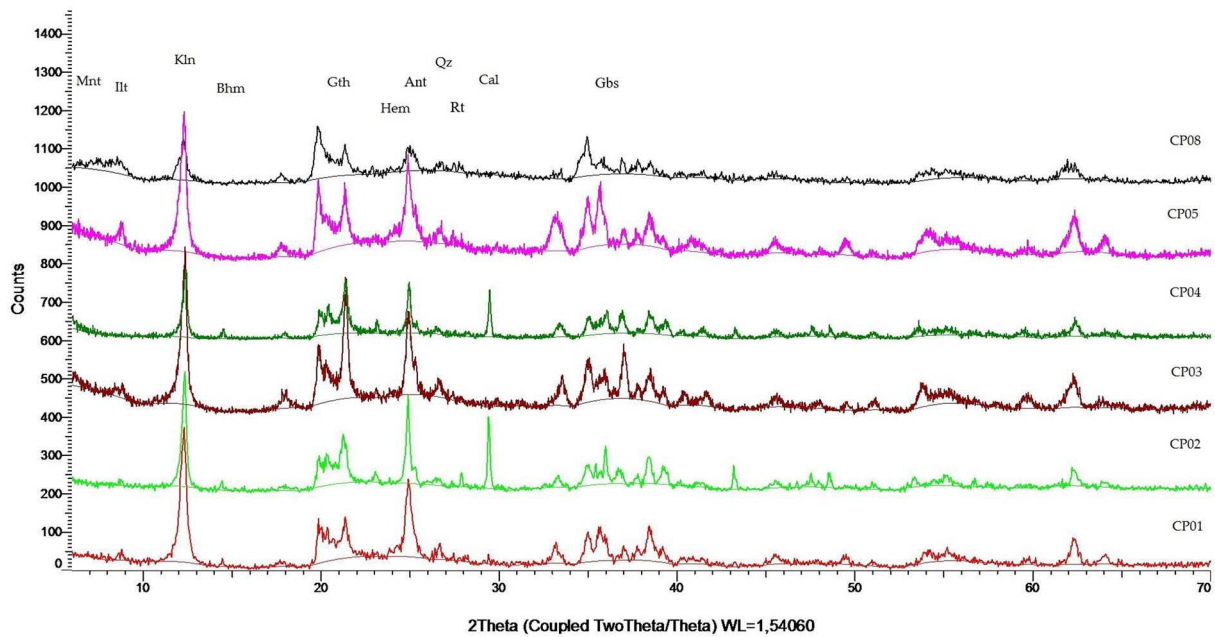

FIGURE 5 | XRPD patterns of representative CP palaeosol samples. Legend. Kln, Kaolinite; Ilt, Illite; Mnt, Montmorillonite; Plg, Palygorskite; Qz, Quartz; Fsp, Feldspar; Cal, Calcite; Rt, Rutile; Ant, Anatase; Hem, Hematite; Gth, Goethite; Gbs, Gibbsite; Bhm, Boehmite; Hl, Halite.
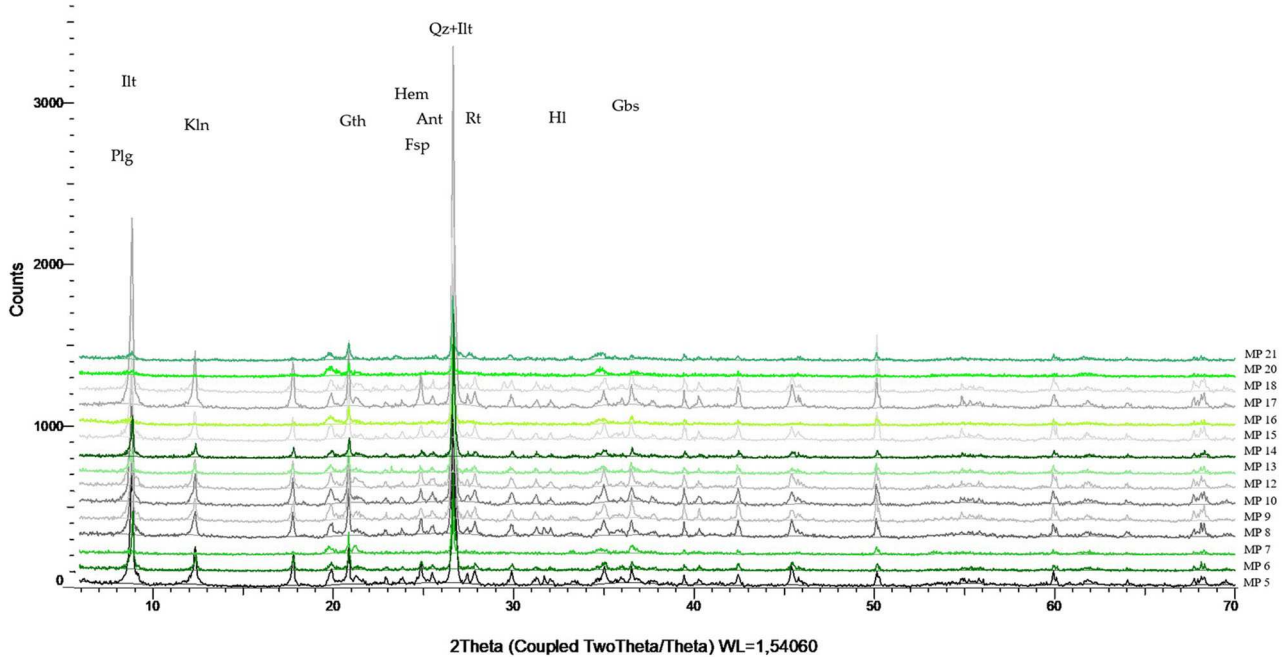

FIGURE 6 | XRPD patterns of representative MP palaeosol samples. Legend. See **Figure 5**.

TABLE 1 | Chemical compositions of the analyzed samples.

Samples		CP01	CP02	CP03	CP04	CP05	CP06	CP07	CP08	CP09	CP10	CP11	CP12	Mean	Median	σ
wt%	D.L.															
Al_2O_3	0.01	31.64	27.00	29.43	28.07	29.02	26.73	25.59	27.85	25.18	24.32	25.49	23.44	26.98	26.87	2.35
CaO	0.01	0.72	4.51	0.24	4.70	0.25	0.37	0.37	0.50	0.34	0.42	0.41	0.85	1.14	0.42	1.63
$Fe_2O_3(T)$	0.01	13.64	17.24	17.18	15.14	15.30	11.56	12.54	9.62	10.51	12.33	10.25	7.90	12.77	12.44	3.00
K_2O	0.01	1.01	0.50	1.56	0.25	1.93	3.13	3.72	3.68	3.93	3.73	4.00	4.28	2.64	3.41	1.49
MgO	0.01	0.29	0.42	0.89	0.47	0.84	1.41	1.59	1.54	1.78	1.65	2.02	2.11	1.25	1.48	0.64
MnO	0.001	0.009	0.049	0.018	0.077	0.020	0.017	0.024	0.006	0.022	0.024	0.021	0.015	0.025	0.021	0.019
Na_2O	0.01	0.16	0.14	0.15	0.12	0.19	0.25	0.23	0.20	0.24	0.22	0.21	0.38	0.21	0.21	0.07
P_2O_5	0.01	0.04	0.07	0.06	0.04	0.06	0.05	0.11	0.05	0.09	0.12	0.09	0.08	0.07	0.07	0.03
SiO_2	0.01	36.82	32.09	35.42	34.04	37.52	39.70	39.83	43.94	42.30	40.91	42.93	43.64	39.10	39.77	3.92
TiO_2	0.001	1.722	1.517	1.625	1.203	1.570	1.532	1.444	1.391	1.371	1.308	1.327	1.298	1.442	1.418	0.153
LOI	0.01	12.15	15.25	14.17	16.48	12.88	14.09	13.18	10.31	13.40	13.92	13.25	14.40	13.62	13.66	1.54
Total		98.21	98.78	100.70	100.60	99.57	98.84	98.63	99.07	99.16	98.95	99.99	98.39	99.24	99.01	0.81
SiO_2/Al_2O_3		1.16	1.19	1.20	1.21	1.29	1.49	1.56	1.58	1.68	1.68	1.68	1.86	1.47	1.52	0.24
ppm																
Ba	2	152	66	126	95	190	233	226	198	209	231	203	216	179	201	56
Co	1	9	59	33	23	21	23	19	17	18	21	17	27	24	21	13
Cr	20	190	140	230	300	220	180	180	130	170	170	160	200	189	180	45
Cs	0.5	5.4	4.0	10.0	1.0	12.3	20.5	19.4	22.2	22.7	21.5	21.7	21.3	15.2	20.0	8.1
Cu	1	5	34	4	12	9	6	13	15	10	11	14	95	19	12	25
Ga	1	38	29	30	38	32	42	38	36	38	40	32	35	36	37	4
Hf	0.2	10.7	12.3	13.2	8.5	13.5	11.1	10.2	10.5	10.8	10.7	8.7	7.9	10.7	10.7	1.8
Nb	1	35	35	29	23	30	30	23	35	32	30	22	35	30	30	5
Ni	1	89	265	168	103	167	165	246	98	150	211	122	179	164	166	56
Pb	5	75	30	50	35	111	37	110	87	56	74	42	68	65	62	28
Rb	2	44	37	71	11	94	151	159	191	186	178	184	196	125	155	69
Sc	1	33	27	33	45	36	29	28	26	29	28	27	24	30	29	6
Sr	2	77	33	99	22	118	109	167	84	119	122	111	140	100	110	41
Th	0.1	21.5	23	27.2	26.8	25.6	21	16.6	20.1	19.1	21.1	17.5	19.6	21.6	21.1	3.5
U	0.1	8.1	10.1	8.2	4.1	8.4	6.3	4.8	4	5.6	6.3	4.1	4.9	6.2	6.0	2.0
V	5	342	442	407	310	331	250	272	195	213	298	197	209	289	285	82
Y	1	39	99	105	80	63	91	73	38	142	118	86	54	82	83	31
Zn	1	42	77	76	22	82	120	152	85	142	165	128	181	106	103	50
Zr	2	405	456	398	287	399	438	460	404	433	439	377	333	402	405	51
La	0.1	46.2	227.0	392.0	66.1	118.0	124.0	212.0	60.4	316.0	324.0	184.0	79.3	179.1	154.0	116.7
Ce	0.1	207.0	185.0	463.0	205.0	251.0	670.0	156.0	90.4	208.0	188.0	108.0	108.0	236.6	196.5	167.3
Pr	0.05	9.23	58.60	82.80	23.50	28.40	28.80	59.90	10.70	89.70	91.10	46.70	19.60	45.75	37.75	30.24
Nd	0.1	32.2	210.0	257.0	84.7	102.0	110.0	221.0	34.9	330.0	331.0	173.0	75.8	163.5	141.5	106.3
Sm	0.1	7.2	35.0	46.9	20.5	24.7	25.3	41.2	6.2	62.7	62.1	30.7	15.1	31.5	28.0	19.0
Eu	0.05	1.70	7.47	9.43	4.53	5.36	5.10	7.14	1.34	11.60	11.20	5.52	3.07	6.12	5.44	3.38
Gd	0.1	7.4	31.2	38.7	15.6	19.0	20.4	22.9	5.5	44.6	41.2	21.5	13.4	23.5	21.0	12.9
Tb	0.1	1.4	4.1	4.9	2.5	3.1	3.3	3.2	1.2	5.7	5.4	2.9	2.1	3.3	3.2	1.5
Dy	0.1	8.7	20.6	23.7	15.8	18.2	18.3	17.2	8.0	30.8	28.8	15.3	12.6	18.2	17.7	7.1
Ho	0.1	1.7	3.7	4.5	3.2	3.4	3.4	3.0	1.7	5.5	5.3	2.8	2.4	3.4	3.3	1.2
Er	0.1	5.5	10.4	12.8	9.5	10.1	10.2	9.0	5.9	15.6	15.0	8.1	7.6	10.0	9.8	3.2
Tm	0.05	0.92	1.47	1.80	1.37	1.66	1.62	1.42	1.11	2.11	2.09	1.18	1.09	1.49	1.45	0.39
Yb	0.1	6.4	9.0	10.4	8.3	10.8	10.9	9.5	8.4	12.9	13.0	7.4	7.0	9.5	9.3	2.2
Lu	0.01	0.96	1.31	1.54	1.21	1.68	1.79	1.45	1.31	1.86	1.97	1.10	1.08	1.44	1.38	0.33
∑REE		336.51	804.85	1349.47	461.81	597.4	1033.11	764.91	237.06	1137.07	1120.16	608.2	348.14	733.22	686.56	362.85
$(La/Yb)_{ch}$		4.88	17.04	25.47	5.38	7.38	7.69	15.08	4.86	16.55	16.84	16.80	7.66	12.14	11.38	6.66
$(La/Sm)_{ch}$		4.04	4.08	5.26	2.03	3.01	3.08	3.24	6.13	3.17	3.28	3.77	3.31	3.70	3.29	1.09
$(Gd/Yb)_{ch}$		0.94	2.81	3.02	1.52	1.43	1.52	1.95	0.53	2.80	2.57	2.35	1.55	1.92	1.75	0.80
Eu/Eu*		0.71	0.69	0.68	0.77	0.76	0.69	0.71	0.70	0.67	0.68	0.66	0.66	0.70	0.69	0.04
Ce/Ce*		2.35	0.38	0.60	1.22	1.02	2.63	0.32	0.83	0.29	0.26	0.27	0.64	0.90	0.62	0.81
CIA		91.95		90.82		88.90	82.31	79.39	80.58	78.38	78.37	78.20	73.68	82.26	79.99	6.17

(Continued)

TABLE 1 | Continued

Samples		MP01	MP02	MP03	MP04	MP05	MP06	MP07	MP08	MP09	MP10	MP11	MP12	Mean	Median	σ
wt%	D.L.															
Al_2O_3	0.01	32.66	30.45	26.92	25.42	22.95	22.24	19.70	21.71	21.25	21.80	20.99	21.13	23.94	22.02	4.10
CaO	0.01	0.10	0.10	0.13	0.08	0.08	0.27	0.70	0.61	0.17	0.10	0.20	0.20	0.23	0.15	0.21
$Fe_2O_3(T)$	0.01	1.62	3.69	9.81	7.34	8.31	7.94	9.17	7.98	7.17	7.06	8.17	7.98	7.19	7.96	2.30
K_2O	0.01	5.38	5.06	4.20	4.37	3.79	3.91	3.44	3.68	3.47	3.87	3.65	3.37	4.02	3.83	0.64
MgO	0.01	0.58	0.63	0.98	0.62	0.67	0.72	2.26	0.81	0.54	0.61	0.61	0.64	0.81	0.64	0.47
MnO	0.001	0.006	0.014	0.131	0.014	0.022	0.223	0.258	0.131	0.339	0.095	0.240	0.143	0.135	0.131	0.111
Na_2O	0.01	1.00	0.88	0.65	0.73	1.28	0.55	0.15	1.31	0.69	0.64	0.61	0.66	0.76	0.68	0.32
P_2O_5	0.01	0.07	0.05	0.09	0.06	0.07	0.06	0.08	0.08	0.06	0.06	0.13	0.12	0.08	0.07	0.02
SiO_2	0.01	49.82	50.15	46.38	52.60	53.97	53.79	48.92	54.34	60.47	58.25	56.69	57.16	53.55	53.88	4.19
TiO_2	0.001	1.074	1.068	1.006	1.200	1.065	1.012	0.785	1.034	1.141	1.145	1.101	1.169	1.067	1.071	0.108
LOI	0.01	7.73	7.55	10.00	7.46	6.76	8.62	15.13	8.89	5.67	5.63	7.12	6.32	8.07	7.51	2.57
Total		100.10	99.63	100.30	99.89	98.97	99.34	100.60	100.60	101.00	99.26	99.50	98.89	99.84	99.76	0.69
ppm																
Ba	2	772	695	570	614	896	683	303	626	677	620	636	521	634	631	142
Co	1	2	7	33	7	11	25	40	21	35	16	29	19	20	20	12
Cr	20	120	130	90	120	80	110	130	80	80	80	100	70	99	95	22
Cs	0.5	20.8	18.3	24.0	15.7	11.7	11.2	11.7	12.7	11.6	12.4	10.9	12.0	14.4	12.2	4.3
Cu	1	10	24	43	36	34	27	29	34	31	30	30	30	30	30	8
Ga	1	40	39	34	34	30	28	51	31	29	29	28	29	34	31	7
Hf	0.2	3.2	3.7	5.1	5.4	6.0	6.0	5.8	6.4	6.6	6.0	8.7	7.7	5.9	6.0	1.5
Nb	1	27	27	27	32	20	19	15	22	22	22	20	24	23	22	5
Ni	1	19	21	70	33	54	49	69	79	101	50	50	55	54	52	24
Pb	5	157	29	36	20	35	32	39	40	34	41	42	42	46	38	36
Rb	2	262	239	208	204	176	199	186	185	171	183	190	176	198	188	27
Sc	1	24	24	23	21	21	20	20	20	19	19	19	19	21	20	2
Sr	2	297	197	169	162	138	133	72	138	119	135	128	127	151	137	55
Th	0.1	11.7	13.5	16.1	18.9	18.0	17.7	12.9	17.5	18.7	15.9	24.3	21.3	17.2	17.6	3.6
U	0.1	2.7	2.9	3.4	3.6	3.3	3.9	3.3	3.4	3.7	3.2	4.4	3.9	3.5	3.4	0.5
V	5	161	169	221	160	151	150	216	148	141	144	170	178	167	161	26
Y	1	14	17	25	29	42	35	40	49	52	41	60	50	38	41	14
Zn	1	23	36	107	49	62	88	74	85	90	74	95	99	74	80	26
Zr	2	114	135	188	192	221	186	198	233	240	228	269	294	208	210	51
La	0.1	157.0	32.0	68.1	43.5	61.8	54.1	79.4	59.2	77.3	54.6	93.3	75.7	71.3	65.0	31.7
Ce	0.1	113.0	52.2	134.0	79.5	121.0	121.0	176.0	123.0	144.0	111.0	170.0	156.0	125.1	122.0	35.4
Pr	0.05	19.10	6.51	13.10	9.78	13.60	13.60	18.50	13.20	20.10	12.40	23.60	17.80	15.11	13.60	4.80
Nd	0.1	46.2	22.7	41.4	35.1	49.6	45.1	61.0	48.4	77.9	45.4	78.4	66.0	51.4	47.3	16.6
Sm	0.1	5.2	4.0	6.6	6.2	9.4	9.0	11.4	9.4	15.0	8.8	14.9	12.4	9.4	9.2	3.6
Eu	0.05	0.96	0.81	1.33	1.27	2.03	1.93	2.33	2.12	3.49	2.00	3.16	2.68	2.01	2.02	0.83
Gd	0.1	3.9	3.9	6.2	6.2	8.0	7.7	8.6	8.9	13.8	8.0	12.7	10.4	8.2	8.0	3.1
Tb	0.1	0.5	0.5	0.9	0.9	1.4	1.2	1.3	1.5	2.1	1.3	1.9	1.6	1.3	1.3	0.5
Dy	0.1	2.8	3.2	5.0	5.5	7.8	6.9	7.1	8.1	11.4	7.1	10.8	9.1	7.1	7.1	2.7
Ho	0.1	0.5	0.6	1.0	1.1	1.5	1.4	1.4	1.6	2.1	1.4	2.2	1.7	1.4	1.4	0.5
Er	0.1	1.7	1.9	2.8	3.2	4.4	3.9	4.1	4.6	6.1	4.0	6.2	5.1	4.0	4.1	1.4
Tm	0.05	0.27	0.31	0.45	0.49	0.66	0.59	0.58	0.68	0.90	0.61	0.89	0.75	0.6	0.60	0.20
Yb	0.1	1.8	2.1	3.0	3.2	4.4	3.7	3.5	4.3	5.7	4.0	5.6	4.7	3.8	3.9	1.2
Lu	0.01	0.29	0.32	0.46	0.47	0.63	0.56	0.50	0.62	0.82	0.58	0.83	0.71	0.57	0.57	0.17
∑REE		353.22	131.05	284.34	196.41	286.22	270.68	375.71	285.62	380.71	261.19	424.48	364.64	301.19	285.92	83.68
$(La/Yb)_{ch}$		58.94	10.30	15.34	9.19	9.49	9.88	15.33	9.30	9.16	9.22	11.26	10.88	14.86	10.09	14.06
$(La/Sm)_{ch}$		19.00	5.04	6.49	4.42	4.14	3.78	4.38	3.96	3.24	3.91	3.94	3.84	5.51	4.05	4.33
$(Gd/Yb)_{ch}$		1.76	1.51	1.67	1.57	1.47	1.69	1.99	1.68	1.96	1.62	1.84	1.79	1.71	1.68	0.16
Eu/Eu^*		0.65	0.63	0.64	0.63	0.72	0.71	0.72	0.71	0.74	0.73	0.70	0.72	0.69	0.71	0.04
Ce/Ce^*		0.48	0.85	1.05	0.90	0.98	1.05	1.08	1.03	0.86	1.00	0.85	1.00	0.93	0.99	0.16
CIA		76.64	76.63	77.85	76.13	74.56	75.41	75.09	72.08	76.23	75.46	75.43	76.57	75.67	75.80	1.43

(Continued)

TABLE 1 | Continued

Samples	D.L.	MP13	MP14	MP15	MP16	MP17	MP18	MP19	MP20	MP21	MP22	Mean	Median	σ	Mean T	Median T	σ T
wt%	D.L.																
Al_2O_3	0.01	20.51	20.54	21.26	17.92	20.14	19.47	18.94	19.29	16.65	16.41	19.11	19.38	1.65	21.74	21.13	4.00
CaO	0.01	0.22	0.14	0.11	0.46	0.15	0.96	0.12	0.67	0.51	0.49	0.38	0.34	0.29	0.30	0.20	0.25
$Fe_2O_3(T)$	0.01	7.69	7.67	7.64	8.68	7.08	7.35	7.62	8.85	7.72	4.96	7.53	7.66	1.05	7.34	7.67	1.81
K_2O	0.01	4.02	3.46	3.60	3.44	3.50	3.38	3.29	3.95	5.64	2.91	3.72	3.48	0.74	3.88	3.68	0.69
MgO	0.01	0.99	0.59	0.55	1.94	0.58	0.65	0.69	2.71	2.69	0.51	1.19	0.67	0.90	0.98	0.65	0.71
MnO	0.001	0.027	0.034	0.090	0.152	0.097	0.173	0.171	0.103	0.076	0.048	0.097	0.094	0.054	0.118	0.103	0.090
Na_2O	0.01	0.52	0.60	0.57	0.28	0.80	1.13	1.30	0.17	0.29	0.79	0.65	0.59	0.37	0.71	0.66	0.34
P_2O_5	0.01	0.09	0.07	0.07	0.16	0.08	0.08	0.10	0.08	0.18	0.05	0.10	0.08	0.04	0.09	0.08	0.03
SiO_2	0.01	56.18	57.28	60.81	53.07	59.86	59.13	59.12	48.47	56.00	65.40	57.53	58.20	4.59	55.36	56.00	4.73
TiO_2	0.001	1.213	1.038	1.064	0.803	1.055	1.058	1.052	0.701	0.853	0.970	0.981	1.045	0.152	1.028	1.055	0.134
LOI	0.01	8.78	7.23	5.10	13.01	6.45	6.35	6.69	14.75	9.16	6.70	8.42	6.97	3.13	8.23	7.46	2.78
Total		100.30	98.66	100.90	99.91	99.79	99.72	99.09	99.74	99.76	99.25	99.71	99.75	0.62	99.78	99.76	0.65
ppm																	
Ba	2	484	488	533	300	611	642	529	251	326	525	469	507	133	559	570	159
Co	1	10	9	14	20	32	32	24	21	16	7	19	18	9	20	20	11
Cr	20	140	120	80	90	70	70	80	120	100	80	95	85	24	97	90	23
Cs	0.5	11.8	10.1	12.5	10.4	12.2	11.8	10.0	12.0	9.2	8.8	10.9	11.1	1.3	12.8	11.8	3.7
Cu	1	27	26	31	30	30	36	29	30	14	24	28	30	6	29	30	7
Ga	1	27	26	29	24	28	28	25	51	36	23	30	28	8	32	29	8
Hf	0.2	7.5	7.6	6.5	6.3	6.9	6.5	7.8	5.5	4.7	10.8	7.0	6.7	1.6	6.4	6.4	1.6
Nb	1	23	19	21	16	21	21	27	13	15	18	19	20	4	21	21	5
Ni	1	43	40	66	55	61	84	54	67	54	39	56	55	14	55	54	19
Pb	5	14	21	30	31	43	63	27	37	14	35	32	31	15	39	35	28
Rb	2	193	171	174	162	165	166	160	195	154	150	169	166	15	185	183	27
Sc	1	19	18	19	17	18	18	16	20	15	14	17	18	2	19	19	3
Sr	2	117	122	128	75	129	125	126	67	91	105	109	120	23	132	128	48
Th	0.1	19.8	22.5	18.5	13.9	19.9	18.0	22.9	13.0	10.3	20.3	17.9	19.2	4.2	17.5	18.0	3.8
U	0.1	3.9	3.5	3.2	3.3	3.6	3.7	3.8	3.2	2.3	4.1	3.5	3.6	0.5	3.5	3.5	0.5
V	5	142	132	138	156	132	134	134	208	133	103	141	134	27	156	150	29
Y	1	39	38	43	35	46	54	46	48	33	35	42	41	7	40	40	11
Zn	1	72	84	68	86	84	92	93	69	68	121	84	84	16	78	84	22
Zr	2	248	272	240	217	254	240	283	191	164	355	246	244	52	226	228	54
La	0.1	61.8	82.2	66.1	61.3	66.9	61.8	80.2	44.2	47.0	70.4	64.2	64.0	12.2	68.1	66.1	24.6
Ce	0.1	123.0	162.0	131.0	107.0	142.0	131.0	153.0	148.0	95.4	144.0	133.6	136.5	20.7	129.0	131.0	29.3
Pr	0.05	13.40	19.10	15.10	14.70	15.40	13.70	19.20	11.60	10.70	15.90	14.88	14.90	2.78	15.00	14.70	3.93
Nd	0.1	45.0	64.6	54.7	50.1	56.2	50.5	71.4	41.5	36.1	51.7	52.2	51.1	10.4	51.8	50.1	13.8
Sm	0.1	8.7	12.2	10.2	9.7	10.7	9.7	12.5	9.8	7.4	9.8	10.1	9.8	1.5	9.7	9.7	2.8
Eu	0.05	1.90	2.45	2.19	2.10	2.35	2.19	2.57	2.21	1.69	2.01	2.17	2.19	0.26	2.08	2.10	0.63
Gd	0.1	7.5	9.0	8.6	8.0	9.3	9.2	12.0	9.5	7.0	7.8	8.8	8.8	1.4	8.5	8.5	2.4
Tb	0.1	1.3	1.3	1.4	1.1	1.5	1.5	1.6	1.4	1.1	1.3	1.4	1.4	0.2	1.3	1.3	0.4
Dy	0.1	7.6	7.7	7.8	6.3	8.5	8.2	9.0	8.4	6.1	7.4	7.7	7.8	0.9	7.4	7.6	2.1
Ho	0.1	1.6	1.6	1.5	1.3	1.7	1.6	1.7	1.7	1.2	1.5	1.5	1.6	0.2	1.5	1.5	0.4
Er	0.1	4.7	4.6	4.3	3.7	4.9	4.8	4.9	4.8	3.5	4.6	4.5	4.7	0.5	4.2	4.4	1.1
Tm	0.05	0.70	0.68	0.65	0.55	0.73	0.70	0.73	0.67	0.49	0.67	0.66	0.68	0.08	0.63	0.66	0.16
Yb	0.1	4.5	4.3	4.2	3.4	4.7	4.4	4.7	4.0	2.9	4.1	4.1	4.3	0.6	4.0	4.1	1.0
Lu	0.01	0.64	0.62	0.62	0.48	0.67	0.65	0.69	0.59	0.45	0.65	0.61	0.63	0.08	0.58	0.62	0.14
$\sum REE$		282.34	372.35	308.36	269.73	325.55	299.94	374.19	288.37	221.03	321.83	306.37	304.15	46.11	303.54	299.94	67.72
$(La/Yb)_{ch}$		9.28	12.92	10.64	12.18	9.62	9.49	11.53	7.47	10.95	11.60	10.57	10.79	1.62	12.91	10.64	10.46
$(La/Sm)_{ch}$		4.47	4.24	4.08	3.98	3.94	4.01	4.04	2.84	4.00	4.52	4.01	4.02	0.46	4.83	4.04	3.24
$(Gd/Yb)_{ch}$		1.35	1.70	1.66	1.91	1.60	1.69	2.07	1.92	1.96	1.54	1.74	1.70	0.22	1.73	1.69	0.19
Eu/Eu*		0.72	0.71	0.71	0.73	0.72	0.71	0.64	0.70	0.72	0.70	0.71	0.71	0.02	0.70	0.71	0.04
Ce/Ce*		1.00	0.96	0.97	0.84	1.04	1.05	0.91	1.53	1.00	1.01	1.03	1.00	0.19	0.97	1.00	0.18
CIA		73.71	76.12	76.36	73.70	74.76	70.47	72.66	72.49	62.66	72.21	72.51	73.18	3.90	74.24	75.09	3.19

$(La/Yb)_{ch} = (La/La_{ch})/(Yb/Yb_{ch})$; $(La/Sm)_{ch} = (La/La_{ch})/(Sm/Sm_{ch})$; $(Gd/Yb)_{ch} = (Gd/Gd_{ch})/(Yb/Yb_{ch})$; $Eu/Eu^* = Eu/Eu_{ch}/\sqrt{(Sm/Sm_{ch} \times Gd/Gd_{ch})}$; $Ce/Ce^* = Ce/Ce_{ch}/\sqrt{(La/La_{ch} \times Pr/Pr_{ch})}$. D.L., Detection Limit. In red are reported mean, median and standard deviation relative to the whole CP and MP sample sets, respectively; in blue are reported mean, median and standard deviation relative to upper and lower sub-sets of the MP palaeosol.

wt.% K_2O (mean = 2.64 wt.%), 0.12–0.38 wt.% Na_2O (mean = 0.21 wt.%), and 0.29–2.11 wt.% MgO (mean = 1.25 wt.%). Two samples yield relatively high CaO concentrations (>4.50 wt.%) due to the presence of carbonate (calcite) fragments, which were detected in XRD patterns.

MP samples, as a whole, yield SiO_2 concentrations of 46.38–65.40 wt.% (mean = 55.36 wt.%; n = 22), lower than UCC and PAAS. The samples contain 16.41–32.66 wt.% Al_2O_3 (mean = 21.74 wt.%), more than the UCC and PAAS. They also contain 1.62–9.81 wt.% Fe_2O_3 (mean = 7.34 wt.%), 2.91–5.64 wt.% K_2O (mean = 3.88 wt.%), 0.08–0.96 wt.% CaO (mean = 0.30 wt.%), and 0.51–2.71 wt.% MgO (mean = 0.98 wt.%). Four samples yield relatively high Na_2O concentrations (>1.10 wt.%) due to the presence of halite, which was detected in XRD patterns.

DISCUSSION AND EVALUATION OF PALAEOWEATHERING

By the comparison of the two alterites the purpose of this work is to obtain information on the parental rock of a palaeosol whose boundary palaeoclimatic conditions are known (CP) and, on the other hand, to get information on the palaeoclimatic conditions from a palaeosol of which, instead, the parent rock is well identified (MP). Beyond the mechanisms of alteration, the cross-comparison of the mineralogical and geochemical features of the two alterites can reveal new insights on the Cretaceous palaeogeographic frame of the south European margin and, on the other end, add new constraints on the climatic scenario during Messinian time.
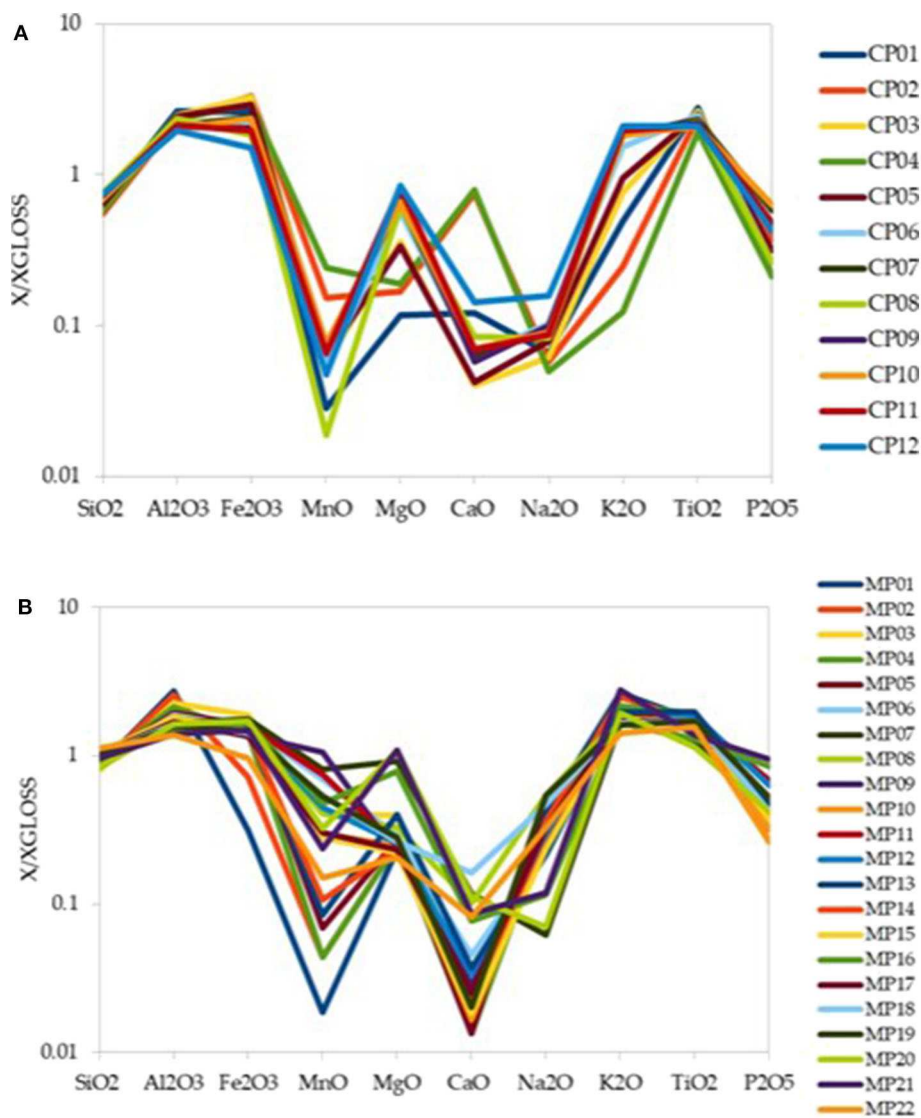
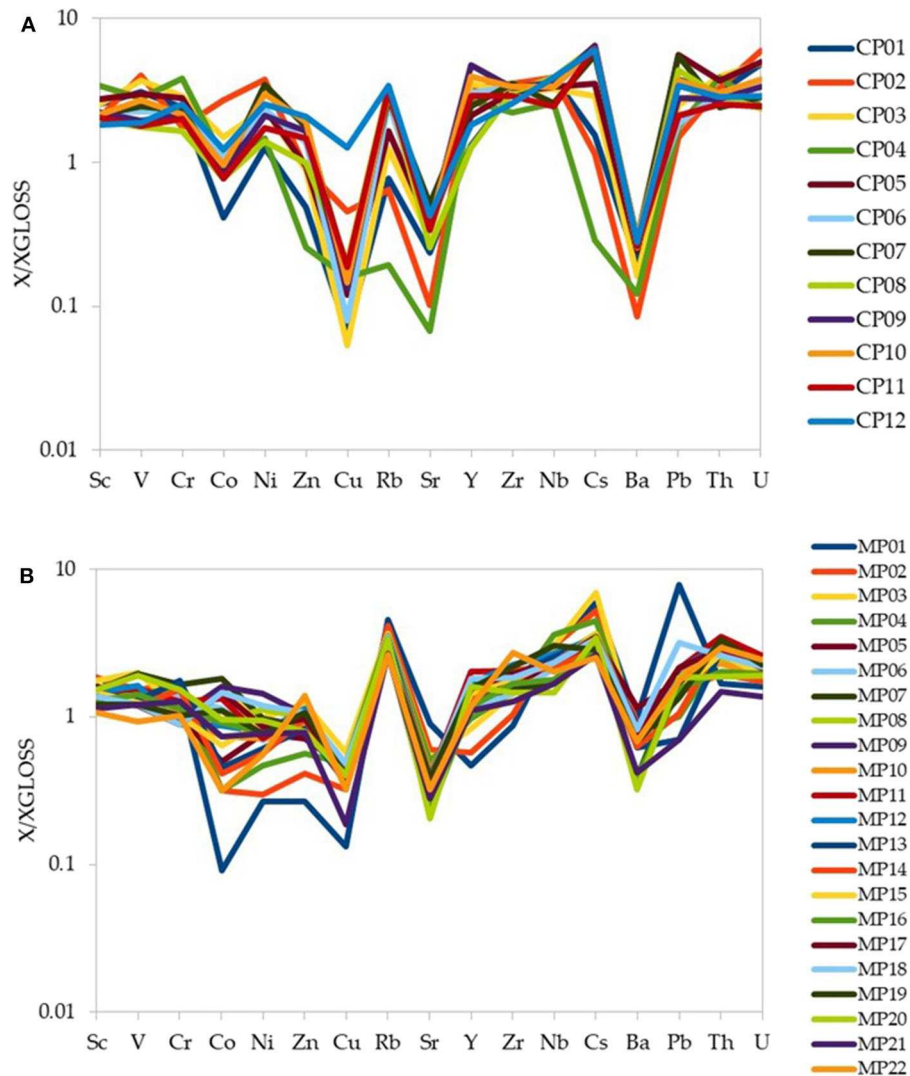**FIGURE 7 |** Global Subducting Sediment (GLOSS)-normalized major elements patterns of **(A)** the CP palaeosols, and **(B)** the MP palaeosols. GLOSS values are from Plank and Langmuir (1998).

In fact few is known about the mechanism that drove the emergence of the Mesozoic shelf at the beginning of Upper Cretaceous (Albian-Turonian) generating bauxite and associated palaeosols. Eustatism and tectonics could both account for such emergence (Durand et al., 1988; Combes and Peybernes, 1991; Haq and Huber, 2017; JeŽ and Otoničar, 2018). In the first case the thick carbonate shelf must have experienced weak erosion; whereas in the second case an important uplift could have caused the complete erosion of the carbonate covers leading to the exposition of the basement.

Uncertainties also affect the Messinian scenario dominated by the salinity crisis (Gardner, 1970) for which the contribute of a warm-dry climate was generally invoked (Suc and Bessais, 1990), even if some authors claim that tectonics is the only cause (Fauquette et al., 2006; Achalhi et al., 2016). In any case the shift to a wetter climate is supposed only at the end of this age (Griffin, 2002; Willett et al., 2006).

Below, the results related to the mineral phases, the major, and trace elements are discussed separately, in the light of their contribution in clarifying the relationships between weathering conditions and precursors in the formation of residual rocks as well as in palaeoclimatic and palaeogeographic reconstructions.

Major Elements Variations and Mineral Phases

We observed several differences between the compositions of the Cretaceous and Messinian palaeosols. The Cretaceous samples yield high TiO_2, Al_2O_3, Fe_2O_3, MgO, and CaO concentrations, whereas the Messinian samples yield higher concentrations of SiO_2, Na_2O, and K_2O (**Figures 7A,B**).

These differences, which include variations in both aluminum and alkaline element concentrations, affect the CIA values. The lower Messinian palaeosol yields a mean CIA of 72.51 (median = 73.18; σ = 3.90), the upper palaeosol yields a slightly higher CIA of 75.67 (median 75.80; σ = 1.43). These values indicate a moderate/intermediate degree of weathering, whereas Cretaceous samples yield a mean CIA of 82.26 (median = 79.99; σ = 6.17), suggesting more intense weathering, according to the different mineralogical evolution (illite rich vs. kaolinite dominated). These inferences are supported by the different proportions of kaolinite and illite in the two sets of samples. On an Al_2O_3– CaO + Na_2O–K_2O diagram (**Figure 8**), the Cretaceous samples plot along a weathering trend parallel to the A–K join moving toward the A apex, indicating the leaching of alkaline elements from primary minerals coupled with the transformation of metamorphic phyllosilicates to kaolinite and in turn to Al-hydroxides (Yuste et al., 2015, 2017). In contrast, most of the Messinian palaeosols samples plot along a weathering trend that is sub-parallel to the A–CN join, indicating the leaching of Ca and Na from primary minerals coupled with the formation of 2:1 phyllosilicates. More in general, the A-CN-K diagram of both the CP and MP subsets clearly show weathering trends moving from a pristine "granitoid," UCC-like, composition toward a clayey composition devoid of Ca and Na. Trends parallel to the A–K join moving toward the K apex are not observed, thus excluding any K-metasomatism modification. This in consistent with the SEM-EDS observations showing that illite and muscovite are always detrital.

The observed mineral distribution in the Messinian alterites is consistent with the hypothesis that weathering intensity was greatest at the surficial palaeosol and diminishes with depth. These characteristics, together with the occurrence of palygorskite, in the lower palaeosol indicate that the initial stage of weathering occurred under semi-arid conditions (Elidrissi et al., 2018 and references therein).

FIGURE 8 | A–CN–K diagram for the analyzed palaeosols. Pl, plagioclase; Gr, granite; Ms, muscovite; Il, illite. The Cretaceous sediments display a typical intense weathering trend, whereas the Messinian samples display a trend consistent with a moderate degree of weathering.
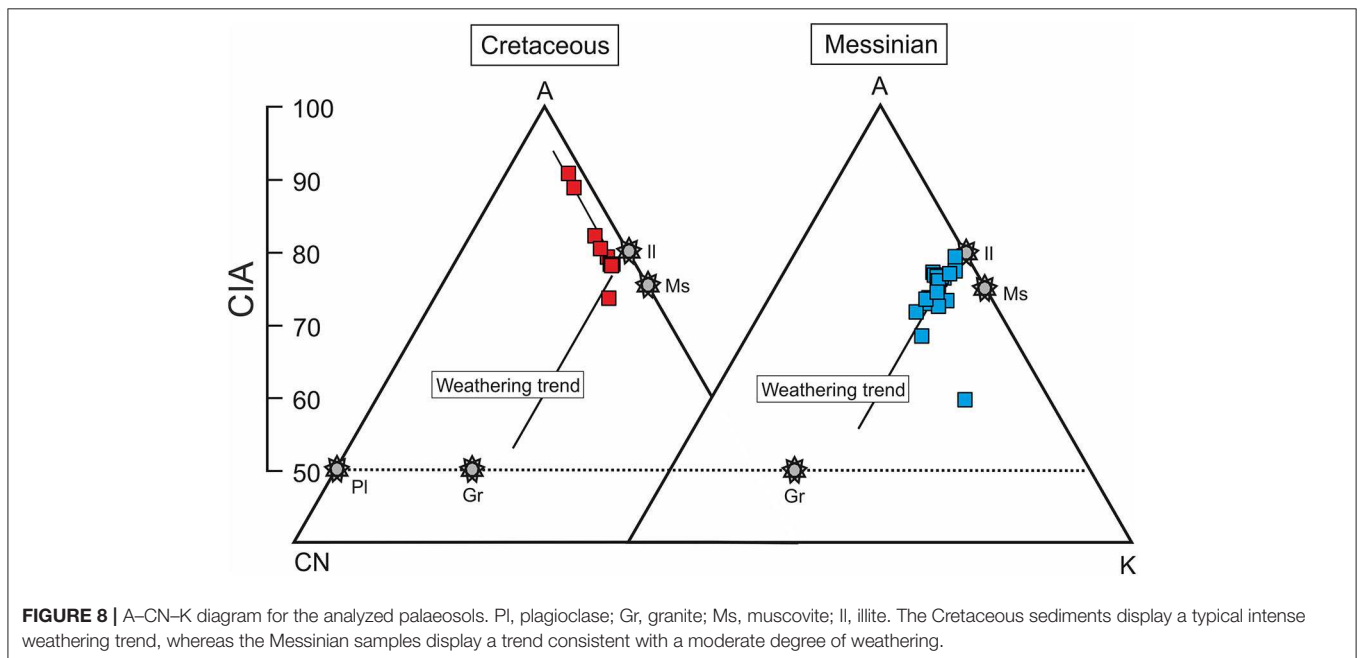
Noticeably the clay of the stratigraphically higher, Messinian, palaeosol contains non-negligible amount of gibbsite. This indicates a high water/rock ratio and the dissolution of kaolinite rather than the direct formation of gibbsite from feldspars, which requires a pH of ~3 (Gardner, 1970), which is inconsistent with the composition of meteoric water in NW Sardinia (present-day pH = 7–9; Mongelli et al., 2013) draining calcareous formations. Kaolinite, instead, could have formed by direct weathering of the basement rocks, before being transported, together other clay minerals, in the form of mud and debris flows, over the Mesozoic carbonate succession, where further weathering generated the kaolinite rich palaeosols. A high water content in the Messinian palaeosol is also testified by the occurrence of magnetite.

Trace Elements Variations

The Cretaceous palaeosols yield higher median concentrations of most trace elements (including Ga), transition metals (V, Cr, Ni, and Zn), high field-strength elements [HFSE; Y, Zr, Nb, total REE

($\sum$REE), Hf, Th, and U] Cs, and Pb than the Messinian samples. In contrast, the Messinian palaeosols are decidedly enriched only in Ba and Cu relative to the Cretaceous samples (**Table 1**).

Both sets of samples yield median concentrations of HFSE, U, large ion lithophile elements (LILE; Rb, Cs, and Pb), and some transitions metals (Sc, V, Cr, and, in the Cretaceous set only, Ni) that are higher than those of average global subducting sediment (GLOSS; Plank and Langmuir, 1998). In contrast, Cu, Sr, and Ba are depleted relative to GLOSS (**Figures 9A,B**).

Chondrite-normalized patterns for both sets of samples (**Figures 10A,B**) display a similar degree of LREE–HREE (Light Rare Earth Elements and Heavy Rare Earth Elements respectively) fractionation, as indicated by their median $(La/Yb)_N$ values (CP = 11.38; MP = 10.64), which are higher than that of GLOSS (7.05). In contrast, the degrees of LREE–MREE (Medium Rare Earth Elements) [median $(La/Sm)_N$: CP = 3.29; MP = 4.04] and MREE–HREE fractionation [median $(Gd/Yb)_N$: CP = 1.75; MP = 1.69] are similar to those of GLOSS (3.14 and 1.67, respectively). The palaeosols yield median Eu

FIGURE 9 | GLOSS-normalized trace elements patterns of **(A)** the CP palaeosols, and **(B)** the MP palaeosols. GLOSS values are from Plank and Langmuir (1998).
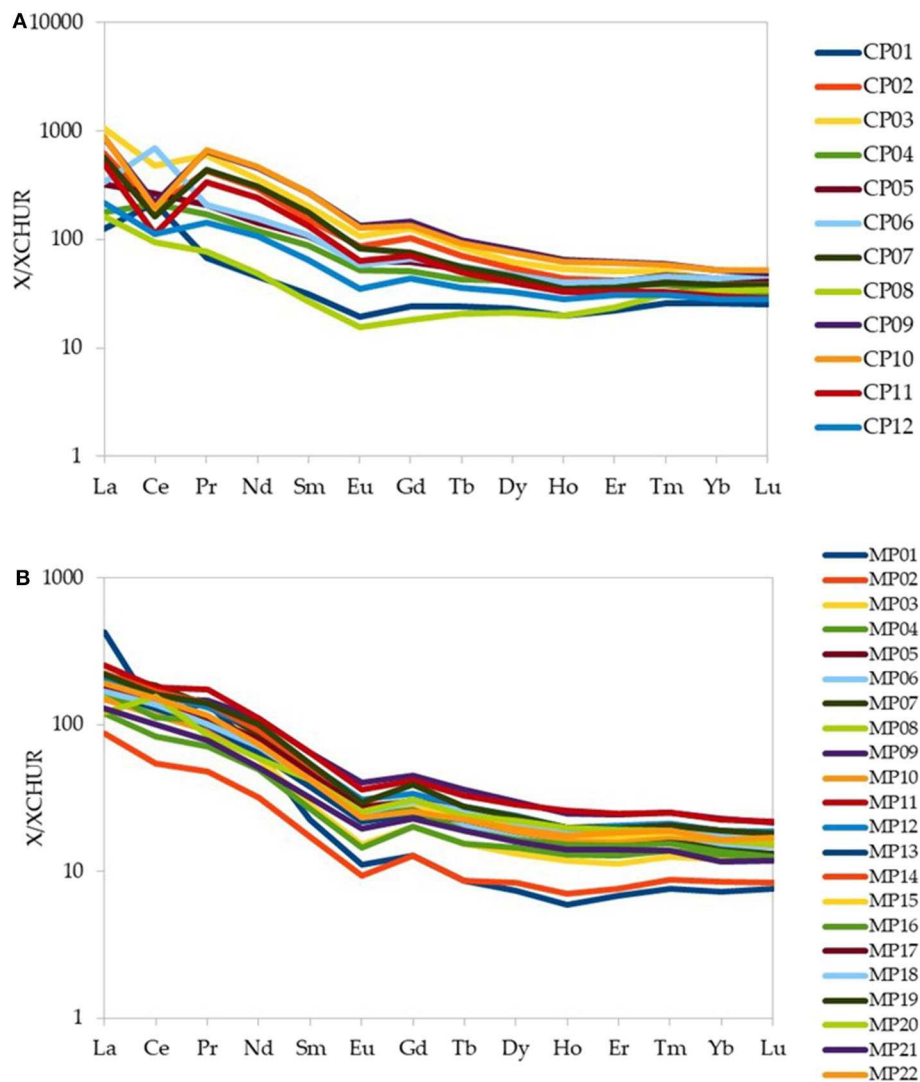
FIGURE 10 | Chondrite-normalized REE patterns of **(A)** the CP palaeosols, and **(B)** the MP palaeosols. Chondrite values are from Taylor and McLennan (1981).

anomalies (Eu/Eu*) (CP = 0.69; MP = 0.71) that are similar to that of GLOSS (0.72). These fractionation indexes, that are those more affected by provenance, especially the Eu/Eu* ratio, suggest both the sets share a provenance characterized by a composition close to the average Upper Continental Crust one.

Finally, the Messinian palaeosols yield Ce anomalies that are generally close to 1 with the exception of sample MP1 (Ce/Ce* = 0.48). The Cretaceous samples instead exhibit a wide range of Ce/Ce* values (0.26–2.63) likely as a consequence of local Eh fluctuations, as supported by the presence of remnants of a reducing humic horizon and oxyhydroxide phases (Braun et al., 1990; Mongelli, 1997; Mameli et al., 2008).

Inter-elemental Relationships

The relationships between major and trace elements in the Cretaceous and Messinian samples were evaluated using varimax

rotation and subsequent R-mode factor analysis. We selected different variables for the two datasets due to their differences in chemical evolution and mineralogy. Most Cretaceous samples display Ce anomalies; consequently, La (representing the LREE) and Yb (representing the HREE) were included in addition to Ce to enable the evaluation of inter-elemental fractionation among the REE. In contrast, as the Messinian samples lack significant Ce anomalies, we included only total REE. We also included a LILE (Rb) because the most abundant mineral in these samples is a 2:1 phyllosilicate.

Cretaceous Palaeosols

Three factors can explain 77.8% of the total variance in the composition of the Cretaceous palaeosols (**Table 2**).

The first factor (F1) explains 38.1% of the total variance and has positive weightings for Al_2O_3, Sc, Cr, and Th. The Al_2O_3 concentrations are higher in soils with a higher weathering rate,

and are indicative of abundant clay minerals and Al-hydroxides. Al-bearing minerals in soils are also generally coupled with resistate phases that control the abundance of low-solubility elements, such as Sc and Th (e.g., Mongelli et al., 2014a,b), which are characterized by low water/rock partition coefficients (Rudnick and Gao, 2014). As for Cr, it occurs as insoluble Cr_2O_3 over much of its Eh–pH space, although in nature most Cr^{3+} is hosted in chromite, and Cr in soils occurs mainly in the residual immobile fraction (Kabata-Pendias, 2010). Thus, F1 likely represents the capacity of some elements to be concentrated during intense weathering.

The second factor (F2) explains 24.2% of the total variance and has significant positive weightings for Fe_2O_3 and V, and a negative weighting for Ga. The positive weightings for Fe_2O_3 and V suggest that V concentrations in the Cretaceous palaeosols were controlled mainly by Fe-oxyhydroxides. As for Ga, in the Ga–O–H system, it is hosted in söhngeite $Ga(OH)_3$, which is a common compound in soils (Kabata-Pendias, 2010), over much of its Eh–pH space (pH = 6–10 for $a_{Ga} = 10^{-8}$). Therefore, F2 might record competition between Fe- and Ga-hydroxides.

The third factor (F3) explains 15.1% of the total variance and has significant positive weightings for La and Yb. This factor accounts for the processes governing the distribution of REE in the Cretaceous palaeosols, with the notable exception of Ce. In general, soil solution composition is the main factor that drives the differential transport of REE during weathering and pedogenesis (Laveuf and Cornu, 2009 and references therein). HREE form complexes with organic matter (Henderson, 1984; Byrne and Li, 1995; Sonke, 2006) and bicarbonates (Cantrell and Byrne, 1987; Lee and Byrne, 1993; Pourret et al., 2007) that are more stable than those involving LREE, resulting in the preferential leaching of HREE during weathering. The soil solution composition also affects adsorption onto secondary minerals, and the balance of REE concentrations between soil solutions and mineral surfaces is controlled mainly by pH-driven adsorption/desorption reactions. REE are adsorbed onto mineral surfaces as pH increases and LREE are more efficiently adsorbed than HREE (Pourret et al., 2010 and references therein). The order in which REE are adsorbed onto mineral surfaces with increasing pH is as follows: LREE > MREE > HREE, and REE are released from mineral surfaces in the same order during a period of decreasing pH (Gammons et al., 2005; Johannesson et al., 2006; Leybourne and Johannesson, 2008; Welch et al., 2009). Therefore, circa-neutral to acidic soil solutions enhance REE fractionation in soils, explaining the higher $(La/Yb)_N$ and $(La/Sm)_N$ values in the palaeosols relative to GLOSS.

Due to its redox chemistry, Ce is commonly fractionated relative to the other REE in soils and sediments that form through intense weathering (e.g., Mongelli et al., 2014a and references therein). Samples that yield negative Ce anomalies typically acquire their REE budget through the scavenging of Ce-depleted solutions resulting from Ce oxidation and precipitation in an environment devoid of organic matter (Usman, 2008; Mongelli et al., 2015).

Messinian Palaeosols

Four factors can explain 85.0% of the total variance in the composition of Messinian palaeosols (**Table 3**).

The first factor (F1) explains 39.4% of the total variance and has strong positive weightings for Al_2O_3, Sc, and Rb. The 2:1 phyllosilicates formed during weathering; thus, Al_2O_3 concentrations are mainly related to the clay mineral content.

The second factor (F2) explains 22.8% of the total variance and has significant positive weightings for Fe_2O_3, Co, Ni, and Cu. Most transition elements can be adsorbed onto Fe-oxyhydroxides (Usman, 2008); however, Acosta et al. (2011) showed that also Fe-rich mica-like clay minerals such as biotite, chamosite, and chlorite, which occur in the Variscan basement, may control the transition element budget in soils. Thus, F2 accounts for the capacity of Fe-oxyhydroxides and possibly 2:1 clay minerals to host heavy metals in soils.

The third factor (F3) explains 14.7% of the total variance and has significant positive weightings for TiO_2 and Th, and a negative weighting for Ga. In the Messinian palaeosols, the most abundant Ti-bearing mineral is detrital rutile. The relationship

TABLE 2 | R-mode factor analysis results for the CP composition.

	Factor 1	Factor 2	Factor 3
Al_2O_3	0.68		
Fe_2O_3(T)		0.74	
Sc	0.93		
V		0.81	
Cr	0.82		
Ni			
Ga		−0.85	
La			0.80
Ce			
Yb			0.90
Th	0.82		

TABLE 3 | R-mode factor analysis results for the MP composition.

	Factor 1	Factor 2	Factor 3	Factor 4
Al_2O_3	0.91			
Fe_2O_3(T)		0.83		
TiO_2			0.86	
Sc	0.97			
V				
Cr				
Co		0.79		
Ni		0.81		
Cu		0.85		
Ga			−0.81	
Rb	0.91			
Zr				
Th			0.78	
ΣREE				0.94

between Ti and Th may indicate that the abundance of rutile covaries with that of detrital Th-bearing minerals such as monazite. The negative weighting for Ga suggests that it is not present in high concentrations in accessory and detrital phases.

The fourth factor (F4) explains 8.1% of the total variance and has significant positive weightings for REE. Thus, F4 accounts for the processes controlling the REE distribution in the samples.

General Implications About the Palaeoclimate Conditions and Palaegeography

In siliciclastic and residual sediments is generally retained (e.g., Perri and Ohta, 2014; Perri et al., 2015a,b) that relationships among Al_2O_3, Sc, and Rb indicate that these elements covary with the abundance of clay minerals, with Rb likely occurring as interlayer cation. Thus, F1 in MP represents the resistance of some trace elements, including LILE such as Rb, to leaching during a weathering less intense with respect to CP. It is interesting to observe that the factors explaining the higher variance in both the sets (F1 Cretaceous vs. F1 Messinian) support what depicted by the mineralogical composition and the A-CN-K diagrams about the difference in palaeoclimate during the formation of the two different residual clay deposits.

The Eu anomaly, recording in sediments the proportion of exposed crust in the source area (e.g., McLennan et al., 1993; Cullers, 2000; Condie et al., 2001; Roser et al., 2002; Perri et al., 2013; Sinisi et al., 2014), has proved to be an effective and reliable proxy of provenance also during intense weathering (e.g., Mongelli et al., 2014a, 2016). Similarly to the Eu/Eu* proxy, the Sm/Nd ratio reflects chemical differentiation, since only minor fractionation of Sm and Nd occurs during intense tropical weathering (Viers and Wasserburg, 2004) and, as a consequence, the Sm/Nd ratio has been profitably used to determine parental affinities for evolved alterites (Mongelli et al., 2014a, 2016). In the Eu/Eu* vs. Sm/Nd binary diagram (**Figure 11**), both the CP and MP subsets show large similarity and fall close to the average cratonic sediment suggesting that the Variscan basement, which patently was the source of the Messinian alluvial deposits, was also the source of the Cretaceous alterites.

Such evidence implies that during the Cenomanian-Turonian interval a wide region north of Sardinia (in pre-drift coordinates) underwent strong uplift and emergence that caused the erosive elision of the Mesozoic carbonatic shelf (at least, 1.5–2 km thick), leading to the exposition and dismantling of the underlying basement. In Nurra the pre-bauxite sequence was eroded down to the Oxfordian dolostone, causing the elision of about 400 m of carbonatic succession. The chrono-stratigraphic gap matches that of Nerthe in Provence (Masse and Philip, 1976), where more than 600 m of lower Cretaceous deposits were eroded (Guyonnet-Benaize et al., 2010). From this match can be argued that north Sardinia was located on the prolongation of the Durancian isthmus where Turonian bauxite is widespread (Laville, 1981; Combes, 1990). This well known structural high developed between the Vocontian basin to the north and
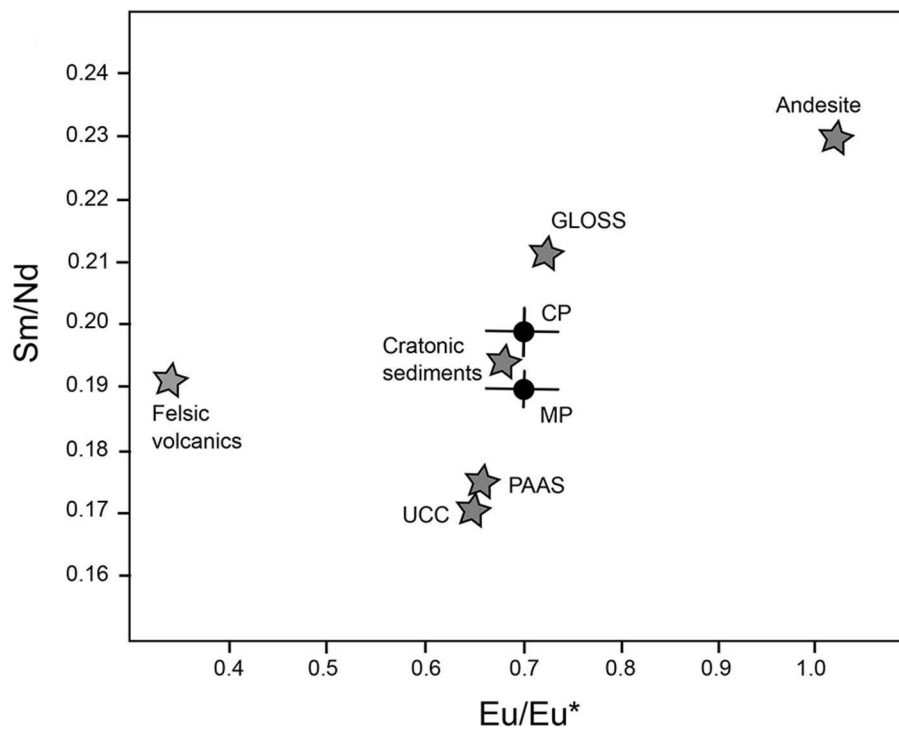
FIGURE 11 | Eu/Eu* vs. Sm/Nd binary plot showing average standard lithologies. Circles are CP and MP palaeosols. Felsic volcanics and Cratonic sediments in Condie (1993); PAAS and Andesite in Taylor and McLennan (1985); GLOSS in Plank and Langmuir (1998).

the South Provencal basin in the south (Masse and Fenerci-Masse, 2013). The trigger for the uplift was recently referred to a wide restraining zone, which caused N–S shortening and long wave E–W crustal folding during the left lateral motion between Iberia and Europe along a huge wrench fault (Schreiber et al., 2011). Eastward, across the Ligure-Piemontese Ocean this fault acted as a trench-trench transform fault separating two oceanic domains with opposite subduction polarity (**Figure 12**; Carmignani et al., 1995; Oggiano et al., 2009). In any case, the uplift was limited to the carbonate cover, hence no bauxite lying directly on basement rocks is known in the Durancian isthmus. And yet, between Sardinia and Provence, there must have been a ridge, with exposed basement, which fed with Al-rich debris the continental plains and the bordering basins. The relics of this structural relief ("Massif Meridional;" Hennuy, 2003) are to be found in the allochthonous slices of basement in the Maure Massive and in basement outcrops buried in the Ligure-Provencal basin (Fournier et al., 2016). Such transpressive ridge faced the beginning subduction of the Ligure-Piemontese Ocean beneath the European plate (Carmignani et al., 1995; Argnani, 2009; Oggiano et al., 2009) and was more elevated—and independent—compared to the Durancian rise (**Figure 12**). The

occurrence of severely uplifted portions of the south European margin are also in agreement with the south Variscan provenance of detrital zircons in both proximal and distal Upper Cretaceous flysches in "Alpine Corsica" (Lin et al., 2018) and in western Liguria (Mueller et al., 2018), respectively. However, the latter authors, disregarding the Cretaceous left lateral motion between Iberia and Europe, refer the uplift, which should have caused the complete elision of the thick Mesozoic cover—and this is not the case—to a lithospheric bulge involving the Var-Maures Massif (i.e., the Durancian isthmus). This bulge is thought caused by the down-bending of the south European margin while it was approaching the Alpin2e accretionary wedge.

To define the degree of weathering of the basement exposed over this structural high is not easy; in fact mantled alterites on the Variscan basement have been hardly spared by the post-Cretaceous erosion, where the protection due to transgressive covers is lacking.

Some residual alterites mantling the Variscan basement, nevertheless, are preserved around the Massif Central; they were classically assigned to the Tertiary (e.g., the siderolithic formation), but palaeomagnetic and thermochronological dating revealed a Cretaceous age (Thiry et al., 2006). Such alterites

FIGURE 12 | Palaeogeographic sketch of Turonian Europe. In the schematic cross section VB, Vocontian Basin; ID, Durancian Isthmus; SPB, South Provencal Basin; TR, Transpressive Belt; NWS, North Western Sardinia and Corsica. The dotted line refers to the base level.
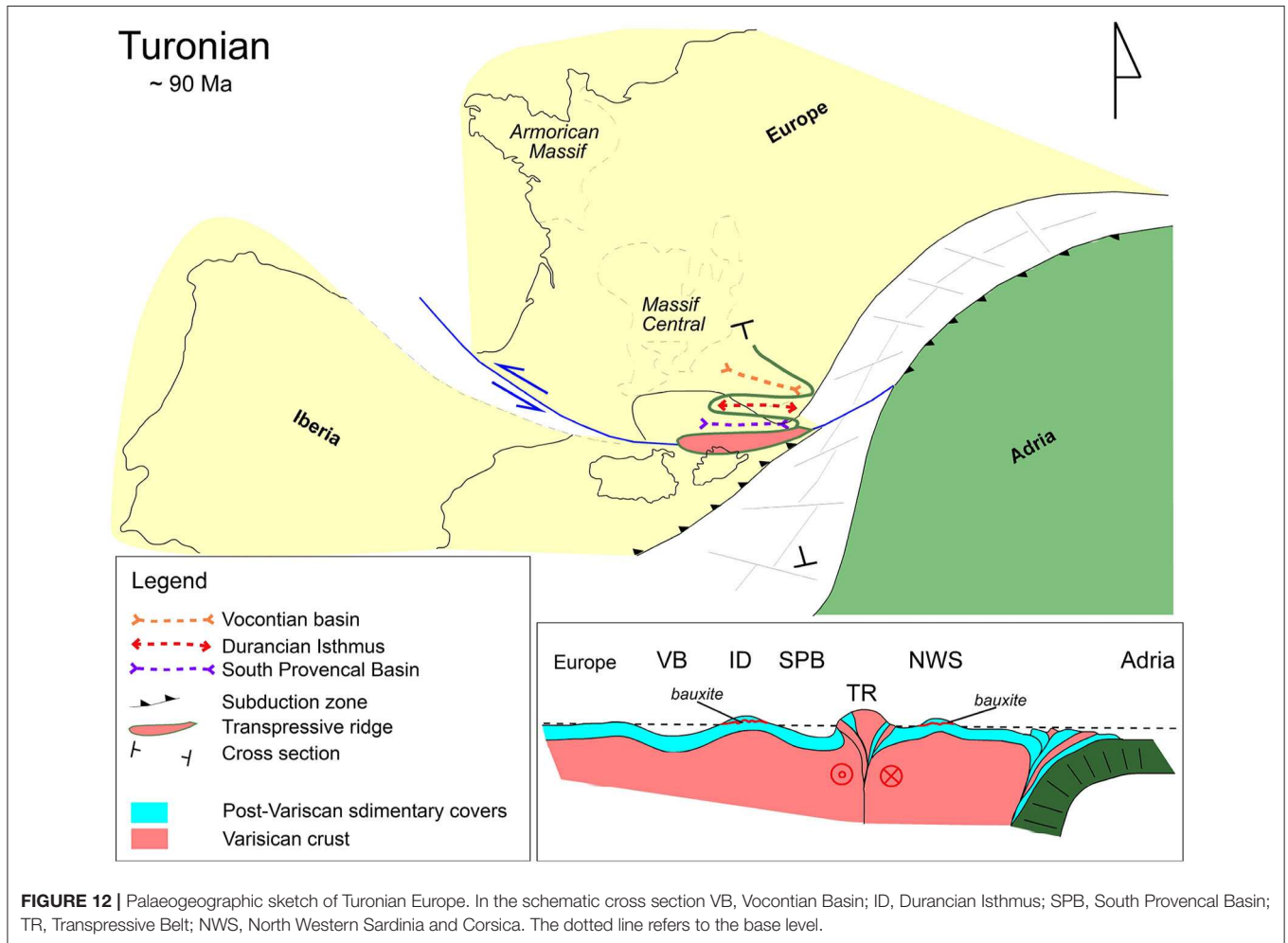
mostly consist of kaolinite and Fe oxy-hydroxides rich paleosols (Simon-Coinçon et al., 2000). A similar, already weathered, material partially contributed to feed the alluvial deposits that evolved into mature palaeosols and then into bauxite over the Upper Cretaceous calcareous palaeosurface (Combes et al., 1993) of Sardinia.

Paleoclimate proxies, including the Ba/Sr ratio and the Na_2O/K_2O molar ratio (Retallack, 1997; Retallack et al., 2001; Sheldon, 2006) support a not negligible water/rock ratio also during the formation of the Messinian deposits. The Ba/Sr ratio is largely used as leaching proxy during weathering since Sr is significantly more soluble than Ba, and Ba/Sr values >2 indicate acidic/leached conditions under wet climate, and in the Messinian upper subset the average value of this proxy is 4.42. Similarly the Na_2O/K_2O index, the proxy measuring the salinization of a palaeosol, is decidedly low (average value 0.17) excluding a dry climate coupled with intense evapo-transpirative condition.

These evidences do not meet the dry Messinian hypothesis (Suc and Bessais, 1990) and suggest a long interval of sub-tropical, wet climate during this age. How long this time span was, in the absence of a continental fossil record, is difficult to establish. In any case it is reasonable to argue that the lower alterite in the alluvial sequence matches one of the dry late Tortonian-early Messinian intervals predating the MSC in the Apennines (Bertini and Menichetti, 2015) and in Southern Spain (Casas-Gallego et al., 2015). The upper palaeosol, indicative of more wet subtropical climate reflects a time span wide enough to encompass the entire MSC, considering that so thick, kaolinite-enriched, paleosols take a few hundred thousand years to be formed (Thiry et al., 2006; Bronger, 2007).

At the Messinian-Pliocene boundary a more seasonal, temperate climate with alternating dry and wet periods prevailed in western Mediterranean (Bertini and Martinetto, 2008). Soil formation was hindered by prevailing erosional dynamics during dry intervals (Günster and Skowronek, 2001). One of these, in north-western Sardinia, could be referred to the gravelly deposit that covers the Messinian alterite.

CONCLUSIONS

Some interesting consequences rise from the comparison of the geochemical and mineralogical features of CP and MP weathering products:

i.   given that the two different alterites sheared a common source, any difference in chemical and mineralogical feature are to be referred to different weathering paths and, ultimately, to different climates;

ii.   during the Cenomanian and Turonian, the Variscan basement was exposed along a possible transpressive belt located between the South Provencal basin and Sardinia;

iii.   the dismantling of this ridge supplied kaolinite-rich material to the emerged Sardinian carbonate platform, where it was converted into a mature palaeosol and, after a long lasting period of alteration driven by monsoonal climate, into bauxite;

iv.   as for the Messinian alterites, the base of the alluvial sequence—possibly late Tortonian-early-Messinian—shows pedogenic clays dominated by illite, palygorskite, and oxidative conditions, which are indicative of dry warm climate, similar to that of actual savannah; conversely the Messinian upper palaeosol yields an unexpected weathering trend toward 2:1 clay minerals and, at less extent, gibbsite that are suggestive of an evolution toward more severe weathering in a wet climate;

v.   MP and CP palaeosols shared similar alteration in the first stages of the weathering path but MP, despite strong Al enrichment, never ended in lateritic soils, and bauxite. Though unexpectedly wet climate was not warm enough to generate ferrallitic alteration.

DATA AVAILABILITY STATEMENT

All datasets presented in this study are included in the article/**Supplementary Material**.

AUTHOR CONTRIBUTIONS

All authors listed have made a substantial, direct and intellectual contribution to the work, and approved it for publication. All authors contributed ideas and assisted with writing and editing the manuscript.

FUNDING

SUPPLEMENTARY MATERIAL

The Supplementary Material for this article can be found online at: https://www.frontiersin.org/articles/10.3389/feart.2020.00290/full#supplementary-material

REFERENCES

Abbazzi, L., Delfino, M., Gallai, G., Trebini, L., and Rook, L. (2008). New data on the vertebrate assemblage of fiume santo (North-western Sardinia, Italy), and overview on the late miocene tusco-Sardinia paleobioprovince. *Palaeontology* 51, 425–451. doi: 10.1111/j.1475-4983.2008.00758.x

Achalhi, M., Münch, P., Cornée, J. J., Azdimousa, A., Melinte-Dobrinescu, M. C., Quillévéré, F., et al. (2016). The late miocene Mediterranean-Atlantic connections through the North rifian corridor: new insights from the boudinar and arbaa taourirt basins (northeastern Rif, Morocco). *Palaeogeogr. Palaeoclimatol. Palaeoecol.* 459, 131–152. doi: 10.1016/j.palaeo.2016.06.040

Acosta, J. A., Martínez-Martínez, S., Faz, A., and Arocena, J. (2011). Accumulations of major and trace elements in particle size fractions of soils on eight different parent materials. *Geoderma* 161, 30–42. doi: 10.1016/j.geoderma.2010.12.001

Anderson, S. P., von Blanckenburg, F., and White, A. F. (2007). Physical and chemical controls on the critical zone. *Elements* 3, 315–319. doi: 10.2113/gselements.3.5.315

Argnani, A. (2009). Plate tectonics and the boundary between alps and apennines. *IJG* 128, 317–330. doi: 10.3301/IJG.2009.128.2.317

Bauluz, B., Yuste, A., Mayayo, M. J., and Canudo, J. I. (2014). Early kaolinization of detrital Weald facies in the galve sub-basin (Central Iberian Chain, north-east Spain) and its relationship to palaeoclimate. *Cretaceous Res.* 50, 214–227. doi: 10.1016/j.cretres.2014.03.014

Bertini, A., and Martinetto, E. (2008). Messinian to Zanclean vegetation and climate of Northern and Central Italy. *Boll Soc. Paleontol. I* 47, 105–121.

Bertini, A., and Menichetti, E. (2015). Palaeoclimate and palaeoenvironments in central Mediterranean during the last 1.6 Ma before the onset of the Messinian Salinity Crisis: a case study from the Northern Apennine foredeep basin. *Rev. Palaeobot. Palyno.* 218, 106–116. doi: 10.1016/j.revpalbo.2014.08.011

Brantley, S. L., White, T. S., White, A. F., Sparks, D., Richer, D., Pregitzer, K., et al. (2006). *Frontiers in Exploration of the Critical Zone, Report of a Workshop Sponsored by the National Science Foundation* (NSF). Newark: NSF.

Braun, J. J., Pagel, M., Muller, J. P., Bilong, P., Michard, A., and Guillet, B. (1990). Cerium anomalies in lateritic profiles. *Geochim. Cosmochim. Acta* 54, 781–795. doi: 10.1016/0016-7037(90)90373-S

Bronger, A. (2007). Time dependence of the rate and direction of mineral weathering and clay mineral formation with special consideration to kaolinites. *RMCG.* 24, 510–523.

Byrne, R., and Li, B. (1995). Comparative complexation behavior of the rare earths. *Geochim. Cosmochim. Acta* 59, 4575–4589. doi: 10.1016/0016-7037(95)00303-7

Cantrell, K. J., and Byrne, R. H. (1987). Rare earth element complexation by carbonate and oxalate ions. *Geochim. Cosmochim. Acta* 51, 597–605. doi: 10.1016/0016-7037(87)90072-X

Carmignani, L., Decandia, F. A., Disperati, L., Fantozzi, P. L., Lazzarotto, A., Liotta, D., et al. (1995). Relationships between the tertiary structural evolution of the sardinia-corsica-provencal domain and the northern apennines. *Terra Nova* 7, 128–137. doi: 10.1111/j.1365-3121.1995.tb00681.x

Carmignani, L., Funedda, A., Oggiano, G., and Pasci, S. (2004). Tectono-sedimentary evolution of southwest Sardinia in the paleogene: pyrenaic or apenninic dynamic? *Geodin. Acta* 17, 275–287. doi: 10.3166/ga.17.275-287

Carmignani, L., Oggiano, G., Funedda, A., Conti, P., and Pasci, S. (2016). The geological map of Sardinia (Italy) at 1:250,000 scale. *J. Maps* 5, 826–835. doi: 10.1080/17445647.2015.1084544

Casas-Gallego, M., Lassaletta, L., Barrón, E., Bruch, A.A., and Montoya, P. (2015). Vegetation and climate in the eastern Iberian Peninsula during the pre-evaporitic Messinian (late Miocene). Palynological data from the Upper Turolian of Venta del Moro (Spain). *Rev Palaeobot. Palyno.* 215, 85–99. doi: 10.1016/j.revpalbo.2015.01.001

Combes, P. J. (1990). Typologie, cadre géodynamique et genèse des bauxites françaises. *Geodin. Acta* 4, 91–109. doi: 10.1080/09853111.1990.11105202

Combes, P. J., Oggiano, G., and Temussi, I. (1993). Geodynamique des bauxites sardes, typologie, g?nese et controle paleotectonique. *C. R. Acad. Sci. II.* 316, 403–409.

Combes, P. J., and Peybernes, B. (1991). Influence of eustacy on the genesis of the ariege-type bauxites, central pyrenees. *C. R. Acad.Sci. II* 313, 669–676.

Condie, K. C. (1993). Chemical composition and evolution of the upper continental crust: contrasting results from surface samples and shales. *Chem. Geol.* 104, 1–37. doi: 10.1016/0009-2541(93)90140-E

Condie, K. C., Dengate, J., and Cullers, R. L. (1995). Behavior of rare-earth elements in a paleoweathering profile on granodiorite in the front range, Colorado, USA. *Geochim. Cosmochim. Acta* 59, 279–294. doi: 10.1016/0016-7037(94)00280-Y

Condie, K. C., Marais, D. J. D., and Abbott, D. (2001). Precambrian superplumes and supercontinents: a record in black shales, carbon isotopes, and paleoclimates. *Precambrian Res.* 106, 239–260. doi: 10.1016/S0301-9268(00)00097-8

Cuccuru, S., Casini, L., Oggiano, G., and Simula, E. N. (2018). Structure of the castellaccio pluton (Asinara Island, Italy). *J. Maps* 14, 293–302. doi: 10.1080/17445647.2018.1463297

Cullers, R. L. (2000). The geochemistry of shales, siltstones and sandstones of Pennsylvian– permian age, Colorado, USA: implications for provenance and metamorphic studies. *Lithos* 51, 181–203. doi: 10.1016/S0024-4937(99)00063-8

Deepthy, R., and Balakrishnan, S. (2005). Climatic control on clay mineral formation: evidence from weathering profiles developed on either side of the Western Ghats. *J. Earth Syst. Sci.* 114, 545–556. doi: 10.1007/BF02702030

Dercourt, J., Zonenshain, L. P., Ricou, L. E., Kazmin, V. G., Le Pichon, X., Knipper, A. L., et al. (1985). Présentation de 9 cartes paléogéographiques au 1:20.000.000.000eme s'étendant de l'Atlantique au pamir pour la période du Lias a' l'actuel. *BSGF* 5, 637–652. doi: 10.2113/gssgfbull.I.5.637

Durand, M., Avril, G., and Meyer, R. (1988). Paleogeography of the first triassic deposits in the southern external alps: importance of the dauphine-durance ridge. *C. R. Acad.Sci. II* 306, 557–560.

Eggleton, R. A. (2001). *The Regolith Glossary: Surficial Geology, Soils and Landscape.* Canberra, ACT: CRC LEME.

Ehrmann, W., Setti, M., and Marinoni, L. (2005). Clay minerals in cenozoic sediments off cape roberts (McMurdo Sound, Antarctica) reveal palaeoclimatic history. *Palaeogeogr. Palaeoclimatol. Palaeoecol.* 229, 187–211. doi: 10.1016/j.palaeo.2005.06.022

Ehrmann, W. U., and Mackensen, A. (1992). Sedimentological evidence for the formation of an east Antarctic ice sheet in eocene/oligocene time. *Palaeogeogr. Palaeoclimatol. Palaeoecol.* 93, 85–112. doi: 10.1016/0031-0182(92)90185-8

Elidrissi, S., Daoudi, L., and Fagel, N. (2018). Palygorskite occurrences and genesis in calcisol and groundwater carbonates of the tensift al haouz area, central Morocco. *Geoderma* 316, 78–88. doi: 10.1016/j.geoderma.2017.12.013

Fauquette, S., Suc, J. P., Bertini, A., Popescu, S. M., Warny, S., Bachiri Taoufiq, N., et al. (2006). How much did climate force the messinian salinity crisis? Quantified climatic conditions from pollen records in the Mediterranean region. *Palaeogeogr. Palaeoclimatol. Palaeoecol.* 238, 281–301. doi: 10.1016/j.palaeo.2006.03.029

Fournier, F., Tassy, A., Thinon, I., Munch, P., Cornee, J.-J., Borgomano, J., et al. (2016). Pre-Pliocene tectonostratigraphic framework of the provence continental shelf (eastern Gulf of Lion, SE France). *BSGF* 187, 187–215. doi: 10.2113/gssgfbull.187.4-5.187

Funedda, A., Oggiano, G., and Pasci, S. (2000). The logudoro basin: a key area for the tertiary tectono-sedimentary evolution of North Sardinia. *Boll. Soc. Geol. Ital.* 119, 31–38.

Gammons, C. H., Wood, S. A., Pedrozo, F., Varekamp, J. C., Nelson, B., Shope, C. L., et al. (2005). Hydrogeochemistry and rare earth element behavior in a volcanically acidified watershed in patagonia, Argentina. *Chem. Geol.* 222, 249-267. doi: 10.1016/j.chemgeo.2005.06.002

Gardner, L. R. (1970). A chemical model for the origin of gibbsite from kaolinite. *Am. Mineralogist* 55, 1380–1389.

Garzanti, E., and Resentini, A. (2016). Provenance control on chemical indices of weathering (Taiwan river sands). *Sediment. Geol.* 336, 81–95. doi: 10.1016/j.sedgeo.2015.06.013

Gattacceca, J., Deino, A., Rizzo, R., Jones, D. S., Henry, B., Beaudoin, B., et al. (2007). Miocene rotation of sardinia: new paleomagnetic and geochronological constraints and geodynamic implications. *EPSL* 258, 359–377. doi: 10.1016/j.epsl.2007.02.003

Griffin, D. L. (2002). Aridity and humidity: two aspects of the late miocene climate of North Africa and the Mediterranean. *Palaeogeogr. Palaeoclimatol. Palaeoecol.* 182, 65–91. doi: 10.1016/S0031-0182(01)00453-9

Günster, N., and Skowronek, A. (2001). Sediment-soil sequences in the Granada Basin as evidence for long- and short-term climatic changes during the Pliocene and Quaternary in the Western Mediterranean. *Quat. Int.* 78, 17–32. doi: 10.1016/S1040-6182(00)00112-9

Guyonnet-Benaize, C., Lamarche, J., Masse, J.-P., Villeneuve, M., and Viseur, S. (2010). 3D structural modelling of small-deformations in poly phase faults pattern, application to the Mid-cretaceous durance uplift, provence (SE France). *J. Geodyn.* 50, 81–93. doi: 10.1016/j.jog.2010.03.003

Haq, B. U., and Huber, B. T. (2017). Anatomy of a eustatic event during the turonian (late cretaceous) hot greenhouse climate. *Sci. China Earth Sci.* 60, 20–29. doi: 10.1007/s11430-016-0166-y

Henderson, P. (1984). *Rare Earth Element Geochemistry (Developments in Geochemistry).* Oxford: Elsevier.

Hennuy, J. (2003). *Dynamique sédimentaire dans un bassin en transtension. Cas du Bassin Sud-Provençal du Turonien moyen au debut du Coniacien moyen* (Ph.D Thesis), Aix-Marseille University, Marseille, France.

Jež, J., and Otoničar, B. (2018). Late cretaceous geodynamics of the northern sector of the adriatic carbonate platform (W Slovenia). *Newsl. Stratigr. Online* 51, 381–410. doi: 10.1127/nos/2018/0439

Jiménez-Moreno, G., Pérez-Asensio, J. N., Larrasoaña, J. C., Aguirre, J., Civis, J., Rivas-Carballo, M. R., et al. (2013). Vegetation, sea-level and climate changes during the Messinian salinity crisis. *GSA Bull.* 125, 432–444. doi: 10.1130/B30663.1

Johannesson, K. H., Hawkins, D. L. Jr., and Cortes, A. (2006). Do archean chemical sediments record ancient seawater rare earth element patterns? *Geochim. Cosmochim. Acta* 70, 871–890. doi: 10.1016/j.gca.2005.10.013

Kabata-Pendias, A. (2010). *Trace Elements in Soils and Plants, 4th Edn.* Boca Raton, FL: CRC Press. doi: 10.1201/b10158

Laveuf, C., and Cornu, S. (2009). A review on the potentiality of rare earth elements to trace pedogenetic processes. *Geoderma* 154, 1–12. doi: 10.1016/j.geoderma.2009.10.002

Laville, P. (1981). La formation bauxitique provençale (France). Séquence des faciès chimiques et paléomorphologie crétacèe. *Chronique Recherche Minière* 461, 51–68.

Lee, J. H., and Byrne, R. H. (1993). Complexation of trivalent rare earth elements (Ce, Eu, Gd, Tb, Yb) by carbonate ions. *Geochim. Cosmochim. Acta* 57, 295–302. doi: 10.1016/0016-7037(93)90432-V

Leybourne, M., and Johannesson, K. (2008). Rare earth elements (REE) and yttrium in stream waters, stream sediments, and Fe-Mn oxyhydroxides: fractionation, speciation, and controls over REE+Y patterns in the surface environment. *Geochim. Cosmochim. Acta* 72, 5962–5983. doi: 10.1016/j.gca.2008.09.022

Lin, W., Rossi, P. H., Faure, M., Li, X. H., Ji, W., and Chu, Y. (2018). Detrital zircon age patterns from turbidites of the balagne and piedmont nappes of alpine corsica (France): evidence for an European margin source. *Tectonophysics* 722, 69–105. doi: 10.1016/j.tecto.2017.09.015

Macias Vazquez, F. (1981). Formation of gibbsite in soils and saprolites of temperate-humid zones. *Clay Miner.* 16, 43–52. doi: 10.1180/claymin.1981.016.1.03

MacLean, W. H., Bonavia, F. F., and Sanna, G. (1997). Argillite debris converted to bauxite during karst weathering: evidence from immobile element geochemistry at the olmedo deposit, Sardinia. *Miner. Deposita* 32, 607–616. doi: 10.1007/s001260050126

Mameli, P., Mongelli, G., Oggiano, G., and Dinelli, E. (2007). Geological, geochemical and mineralogical features of some bauxite deposits from nurra (Western Sardinia, Italy): insights on conditions of formation and parental affinity. *Int. J. Earth Sci.* 96, 887–902. doi: 10.1007/s00531-006-0142-2

Mameli, P., Mongelli, G., Oggiano, G., and Sinisi, R. (2008). Iron concentration in palaeosols and in clayey marine sediments: two case studies in the variscan basement of Sardinia (Italy). *Clay Miner.* 43, 531–546. doi: 10.1180/claymin.2008.043.4.02

Masse, J.-P., and Fenerci-Masse, M. (2013). Drowning events, development and demise of carbonate platforms and controlling factors: the late barremian-early aptian record of Southeast France. *Sediment. Geol.* 298, 28–52. doi: 10.1016/j.sedgeo.2013.09.004

Masse, J.-P., and Philip, J. (1976). Paléogéographie et tectonique du crétacé moyen en Provence. *Rev. Geogr. Phys. Geol. Dyn.* 2, 49–66.

McLennan, S. M., Hemming, D. K., and Hanson, G. N. (1993). Geochemical approaches to sedimentation, provenance and tectonics. *Geol. Soc. Am. Spec. Papers* 284, 21–40. doi: 10.1130/SPE284-p21

Mongelli, G. (1997). Ce-anomalies in the textural components of upper cretaceous karst bauxites from the apulian carbonate platform (southern Italy). *Chem. Geol.* 140, 69–79. doi: 10.1016/S0009-2541(97)00042-9

Mongelli, G., Boni, M., Buccione, R., and Sinisi, R. (2014a). Geochemistry of the apulian karst bauxites (southern Italy): chemical fractionation and parental affinities. *Ore Geol. Rev.* 63, 9–21. doi: 10.1016/j.oregeorev.2014.04.012

Mongelli, G., Buccione, R., Gueguen, R., Langone, A., and Sinisi, R. (2016). Geochemistry of the apulian allochthonous karst bauxite, Southern Italy: distribution of critical elements and constraints on late cretaceous peri-tethyan palaeogeography. *Ore Geol. Rev.* 77, 246–259. doi: 10.1016/j.oregeorev.2016.03.002

Mongelli, G., Mameli, P., Oggiano, G., and Sinisi, R. (2012). Messinian palaeoclimate and palaeo-environment in the western mediterranean realm: insights from the geochemistry of continental deposits of NW Sardinia (Italy). *Int. Geol. Rev.* 54, 971–990. doi: 10.1080/00206814.2011. 588823

Mongelli, G., Mameli, P., Oggiano, G., and Sinisi, R. (2013). Generation of Ce anomalies in SW Sardinian Mn ores. *J. Geochem. Explor.* 133, 42–49. doi: 10.1016/j.gexplo.2012.10.002

Mongelli, G., Paternoster, M., Rizzo, G., and Sinisi, R. (2014b). Trace elements and REE fractionation in subsoils developed on sedimentary and volcanic rocks: case study of the Mt. Vulture area, southern Italy. *Int. J. Earth Sci.* 103, 1125–1140. doi: 10.1007/s00531-014-1003-z

Mongelli, G., Sinisi, R., Mameli, P., and Oggiano, G. (2015). Ce anomalies and trace element distribution in sardinian lithiophorite-rich Mn concretions. *J. Geochem. Explor.* 153, 88–96. doi: 10.1016/j.gexplo.2015.03.004

Mueller, P., Langone, A., Patacci, M., and Di Giulio, A. (2018). Detrital signatures of impending collision: the deep-water record of the upper cretaceous bordighera sandstone and its basal complex (Ligurian Alps, Italy). *Sediment. Geol.* 377, 147–161. doi: 10.1016/j.sedgeo.2018.10.002

National Research Council, N. R. C. (2001). *Basic Research Opportunities in Earth Science.* Washington, DC: National Academy Press.

Nesbitt, H. W., and Markovics, G. (1997). Weathering of granodioritic crust, long-term storage of elements in weathering profiles, and petrogenesis of siliciclastic sediments. *Geochim. Cosmochim. Acta* 61, 1653–1670. doi: 10.1016/S0016-7037(97)00031-8

Nesbitt, H. W., Markovics, G., and Price, R. C. (1980). Chemical processes affecting alkalis and alkaline earths during continental weathering. *Geochim. Cosmochim. Acta* 44, 1659–1666. doi: 10.1016/0016-7037(80)90218-5

Nesbitt, H. W., and Young, G. M. (1982). Early proterozoic climates and plate motions inferred from major element chemistry of lutites. *Nature* 299, 715–717. doi: 10.1038/299715a0

Net, L. I., Alonso, M. S., and Limarino, C. O. (2002). Source rock and environmental control on clay mineral associations, lower section of paganzo group (carboniferous), Northwest Argentina. *Sediment. Geol.* 152, 183–199. doi: 10.1016/S0037-0738(02)00068-4

Oggiano, G., Funedda, A., Carmignani, L., and Pasci, S. (2009). The sardinia-corsica microplate and its role in the tertiary intraplate strike-slip tectonics of Sardinia. *Boll. Soc. Geol. Italy* 128, 527–539. doi: 10.3301/IJG.2009.128.2.527

Oggiano, G., and Mameli, P. (2006). Diamictite and oolitic ironstones, a sedimentary association at ordovician-silurian transition in the North gondwana margin: new evidence from the inner nappe of Sardinia variscides (Italy). *Gondwana Res.* 9, 500–511. doi: 10.1016/j.gr.2005.11.009

Oudet, J., Munch, P. H., Verati, C., Ferrandini, M., Melinte Dobrinescu, M., Gattacceca, J., et al. (2010). Integrated chronostratigraphy of an intra-arcbasin: 40Ar/39Ar datings, micropalaeontology and magnetostratigraphy of the early miocene castelsardo basin (Northern Sardinia, Italy). *Palaeogeogr. Palaeoclimatol. Palaeoecol.* 295, 293–306. doi: 10.1016/j.palaeo.2010.06.007

Perri, F., Critelli, S., Martín-Algarra, A., Martín-Martín, M., Perrone, V., Mongelli, G., et al. (2013). Triassic redbeds in the malaguide complex (betic cordillera—Spain): petrography, geochemistry and geodynamic implications. *Earth Sci. Rev.* 117, 1–28. doi: 10.1016/j.earscirev.2012.11.002

Perri, F., Dominici, R., and Critelli, S. (2015a). Stratigraphy, composition and provenance of argillaceous marls from the calcare di base formation, rossano basin (northeastern Calabria). *Geol. Mag.* 152, 193–209. doi: 10.1017/S0016756814000089

Perri, F., and Ohta, T. (2014). Paleoclimatic conditions and paleoweathering processes on mesozoic continental redbeds from western-central mediterranean alpine chains. *Palaeogeogr. Palaeoclimatol. Palaeoecol.* 395, 144–157. doi: 10.1016/j.palaeo.2013.12.029

Perri, F., Ohta, T., and Critelli, S. (2015b). Characterization of submarine canyon bathymetries in northern Ionian Sea, Italy, using sediment geochemical variation induced by transportation distance and basin depth. *Int. J. Earth Sci.* 104, 1353–1364. doi: 10.1007/s00531-015-1150-x

Peuraniemi, V., and Pulkkinen, P. (1993). Preglacial weathering crust in ostrobothnia, western finland, with special reference to the raudaskyla occurrence. *Chem. Geol.* 107, 313–316. doi: 10.1016/0009-2541(93)90198-R

Philip, J. (1983). Paleobiogeographie des rudistes et geodinamique des marges mèsogeènnès au cretacè supèrièur. *Bull. Soc. Geol. France* 24, 995–1006. doi: 10.2113/gssgfbull.S7-XXIV.5-6.995

Philip, J., Cherchi, A., Schroeder, R., Sigal, J., and Allemann, J. (1978). Les formations à rudistes du crétacé supérieur de Sardaigne. Données

stratigraphiques et paléobiogéographiques. *C.R. Somm. Soc. Geol. France* 2, 83–85.

Plank, T., and Langmuir, C. H. (1998). The chemical composition of subducting sediment and its composition for the crust and mantle. *Chem. Geol.* 145, 325–394. doi: 10.1016/S0009-2541(97)00150-2

Pourret, O., Davranche, M., Gruau, G., and Dia, A. (2007). Competition between humic acid and carbonates for rare earth elements complexation. *J. Colloid Interf. Sci.* 305, 25–31. doi: 10.1016/j.jcis.2006.09.020

Pourret, O., Gruau, G., Dia, A., Davranche, M., and Molenat, J. (2010). Colloidal controls on the distribution of rare earth elements in shallow groundwaters. *Aquat. Geochem.* 16, 31–59. doi: 10.1007/s10498-009-9069-0

Retallack, G. J. (1997). *A Colour Guide to Paleosols.* Chichester: John Wiley and Sons.

Retallack, G. J., Krull, E. S., and Bockheim, J. G. (2001). New grounds for reassessing the palaeoclimate of the sirius group, Antarctica. *J. Geol. Soc. London* 158, 925–935. doi: 10.1144/0016-764901-030

Robert, C., and Maillot, G. (1990). "Paleoenvironments in the weddell sea area and antarctic climates, as deduced from clay mineral associations and geochemical data, ODP Leg 113," in *Proceeding of the Ocean Drilling Program. Science Research*, eds P. F. Barker and J. P. Kennett (College Station, TX: Ocean Drilling Program), 51–70.

Roser, B. P., Coombs, D. S., Korsch, R. J., and Campbell, J. D. (2002). Whole-rock geochemical variations and evolution of the arc-derived murihiku terrane. *N. Z. Geol. Mag.* 139, 665–685. doi: 10.1017/S0016756802006945

Rudnick, R., and Gao, S. (2014). "Composition of the continental crust," in *Treatise on Geochemistry*, eds H. D. Holland and K. K. Turekian *2nd Edn*, Vol. 4 (Amsterdam: Elsevier), 1–51.

Schreiber, D., Giannerini, G., and Lardeaux, J. M. (2011). The Southeast France basin during late cretaceous times: the spatiotemporal link between pyrenean collision and alpine subduction. *Geodin. Acta* 24, 21–35. doi: 10.3166/ga.24.21-35

Sheldon, N. D. (2006). Abrupt chemical weathering increase across the permian-triassic boundary. *Palaeogeogr. Palaeoclimatol. Palaeoecol.* 231, 315–321. doi: 10.1016/j.palaeo.2005.09.001

Simon-Coinçon, R., Thiry, M., and Quesnel, F. (2000). Siderolithic palaeolandscapes and palaeoenvironments in the northern Massif Central (France). *C. R. Acad. Sci. II.* 330, 693–700. doi: 10.1016/S1251-8050(00)00189-0

Singer, A. (1984). The paleoclimatic interpretation of clay minerals in sediments - a review. *Earth-Sci. Rev.* 21, 251–293. doi: 10.1016/0012-8252(84)90055-2

Sinisi, R., Mongelli, G., Mameli, P., and Oggiano, G. (2014). Did the variscan relief influence the permian climate of mesoeurope? Insights from geochemical and mineralogical proxies from Sardinia (Italy). *Palaeogeogr. Palaeoclimatol. Palaeoecol.* 396, 132–154. doi: 10.1016/j.palaeo.2013.12.030

Sonke, R. M. (2006). Lanthanide-humic substances complexation. II. Calibration of humic ion-bonding model V. *Environ. Sci. Technol.* 40, 7481–7487. doi: 10.1021/es060490g

Suc, J-P., and Bessais, E. (1990). Continuous thermo-xeric climate in Sicily before, during and after the Messinian salinity crisis. *C. R. Acad. Sci. II.* 310, 1701–1707.

Taylor, G., and Eggleton, R. A. (2001). *Regolith Geology and Geomorphology: Nature and Process.* Chichester; New York, NY; Weinheim, Brisbane, QLD; Toronto, ON: John Wiley and Sons.

Taylor, S. R., and McLennan, S. M. (1981). The composition and evolution of the continental crust: rare earth element evidence from sedimentary rocks. *Phil. Trans. R. Soc. Lond. A* 301, 381–399. doi: 10.1098/rsta.1981.0119

Taylor, S. R., and McLennan, S. M. (1985). *The Continental Crust: Its Composition and Evolution.* Oxford: Blackwell.

Thiry, M., Quesnel, F., Yans, J., Wyns, R., Vergari, A., Theveniaut, H., et al. (2006). Continental France and Belgium during the early cretaceous: paleoweatherings and paleolandforms. *BSGF.* 177, 155–175. doi: 10.2113/gssgfbull.177.3.155

Thomas, B., and Gennesseaux, M. (1986). A two stage rifting in the basin of the corsica-Sardinia strait. *Marine Geol.* 72, 225–239. doi: 10.1016/0025-3227(86)90121-0

Usman, A. R. A. (2008). The relative adsorption selectivities of Pb, Cu, Zn, Cd and Ni by soils developed on shale in New Valley, Egypt. *Geoderma* 144, 334–343. doi: 10.1016/j.geoderma.2007.12.004

Viers, J., and Wasserburg, G. J. (2004). Behavior of Sm and Nd in a lateritic soil profile. *Geochim. Cosmochim. Acta* 68, 2043–2054. doi: 10.1016/j.gca.2003.10.034

Welch, S. A., Christy, A. G., Isaacson, L., and Kirste, D. (2009). Mineralogical control of rare earth elements in acid sulfate soils. *Geochim. Cosmochim. Acta* 73, 44–64. doi: 10.1016/j.gca.2008.10.017

Willett, S. D., Schlunegger, F., and Picotti, V. (2006). Messinian climate change and erosional destruction of the central European Alps. *Geology* 34, 613–616. doi: 10.1130/G22280.1

Yuste, A., Bauluz, B., and Mayayo, M. J. (2015). Genesis and mineral transformations in lower cretaceous karst bauxites (NE Spain): climatic influence and superimposed processes. *Geol. J.* 50, 839–857. doi: 10.1002/gj.2604

Yuste, A., Bauluz, B., and Mayayo, M. J. (2017). Origin and geochemical evolution from ferrallitized clays to karst bauxite: an example from the lower cretaceous of NE Spain. *Ore Geol. Rev.* 84, 67–79. doi: 10.1016/j.oregeorev.2016.12.025

Zabel, M., Schneider, R. R., Wagner, T., Adegbie, A. T., de Vries, U., and Kolonic, S. (2001). Late Quaternary climate changes in central Africa as inferred from terrigenous input to the Niger fan. *Quaternary Res.* 56, 207–217. doi: 10.1006/qres.2001.2261